Experimental Investigation of Internal Tide Generation by Two-Dimensional Topography using Synthetic Schlieren

by

Paula Echeverri Mondragón

B.S., Aerospace Engineering (2004)
Massachusetts Institute of Technology

Submitted to the Department of Mechanical Engineering
in partial fulfillment of the requirements for the degree of

Master of Science

at the

MASSACHUSETTS INSTITUTE OF TECHNOLOGY

June 2006

Signature of Author ....
Department of Mechanical Engineering
May 12, 2006

Certified by ....
Thomas Peacock
Assistant Professor of Mechanical Enginnering
Thesis Supervisor

Accepted by ....
Lallit Anand
Professor of Mechanical Engineering
Chairperson, Department Committee on Graduate Students

Experimental Investigation of Internal Tide Generation by Two-Dimensional Topography using Synthetic Schlieren

by

Paula Echeverri Mondragón

Submitted to the Department of Mechanical Engineering
on May 12, 2006, in partial fulfillment of the
requirements for the degree of
Master of Science

Abstract

An experimental investigation of internal tide generation at two-dimensional topography was carried out using the synthetic Schlieren experimental technique. Two linear models were tested: Balmforth, Ierley and Young's [1] subcritical solution for a Gaussian ridge and Hurley and Keady's [15] super-critical solution for a knife-edge. The former was modified to account for the effects of viscosity in the propagating wave beams.

The experiment set up comprised a wave-tank with a linear salt-water stratification and a sliding stage on which the topography oscillated horizontally to simulate tidal flow. The wave field was measured by capturing the distortion of a pattern of random dots placed on a light sheet behind the tank using a CCD camera, and using the synthetic Schlieren processing of the movies obtained.

Four experiments were performed, for wave beams propagating close to 25 ° and 56 ° from the horizontal for each topographic feature. The subcritical theory over-predicted the peak disturbance over the Gaussian ridge by a maximum of 50%, and it correctly predicted the profile shape and evolution along the wave beam and throughout one period of the oscillation. The supercritical knife-edge theory predicted the disturbance amplitude, shape and evolution within experimental error. The results showed that at Reynolds numbers below $O(10^5)$, viscosity suppresses nonlinear effects and smoothes out instabilities predicted by inviscid models that would lead to overturning.

These experiments have motivated the construction of a larger wave-tank to achieve higher Reynolds numbers. Future experiments will investigate nonlinear internal tide generation, overturning and mixing in unstable wave beams and flow separation over topography.

Thesis Supervisor: Thomas Peacock
Title: Assistant Professor of Mechanical Enginnering

Contents

List of Figures

Acknowledgements

Many thanks to Professor Thomas Peacock for guiding me through a very inspiring project, for his patience with my writing and for his good spirits throughout much data processing. Mostly, thanks for all the good advice on travel and for making sure we made it to Hawaii.

I am also indebted to Professor Neil Balmforth, who explained the math to us in coffee shops in Woods Hole; to Doctor Ali Tabei, who was always happy to help with the experiments; and to Professor Anette Hossoi and her research group, who invited me to their seminars. The talks were tons of fun and very inspiring; their comments about my research were very kind and helpful. Many people helped put up the experiments and keep them running. Ray Hardin and Leslie Regan helped me keep track of everything in the lab and in regards to my degree; Andrew Gallant put together a beautiful setup; Dave Robertson and Dick Perdichizzi welcomed me again in the Aeronautics and Astronautics department Gelb lab and let me use the foam-cutter. I am very grateful for their support.

The scientists and crew on board the RV-Revelle during the second IWAP 2006 cruise were great hosts. Thanks for showing the tourists how everything works and for making jokes and coffee that kept me happy through the final stages of the writing. I wish you the best of luck finding many Internal Waves Across the Pacific.

My most special thanks go to Carolyn, Rafael, Aboud, Vanessa and Angelica for so much patience, jokes and love.

Chapter 1

Introduction

1.1 The role of internal tides in the deep ocean

Tidal currents flowing back and forth over ocean ridges generate internal gravity wave beams that propagate away from topography, as shown schematically in figure 1-1. This is one of the processes that draws energy from the moon's orbit around the earth, such that the moon recedes from us by a few centimeters every year. The internal wave beams ultimately dissipate and generate mixing, which affects the thermohaline circulation in the ocean. These reasons have sparked a great interest in developing a detailed understanding of internal wave generation by topography, which will improve estimates of energy conversion from the tides and shed light on the subsequent dissipation of internal waves.

The energy transferred from barotropic tidal currents into a baroclinic internal wave field account for a large fraction of energy lost from the tides. The importance of tidal conversion over topography was realized by Egbert and Ray [5], who used Topex/Poseidon satellite altimeter data to constrain a tidal model and localize the rates of energy dissipation from the lunar and solar tides, which had been previously estimated to total 3.7 TW. The distribution of the energy flux from the tides over the ocean surface is shown in figure 1-2. About 1 TW of this occurs in the deep ocean, in particular in regions with large topographic features, where the tidal dissipation measured is much larger than the estimated dissipation due to bottom friction only. These observations have been investigated further, for instance by Merrifield and Holloway [25], who used the Princeton Ocean Model (POM) to do a numerical simulation of

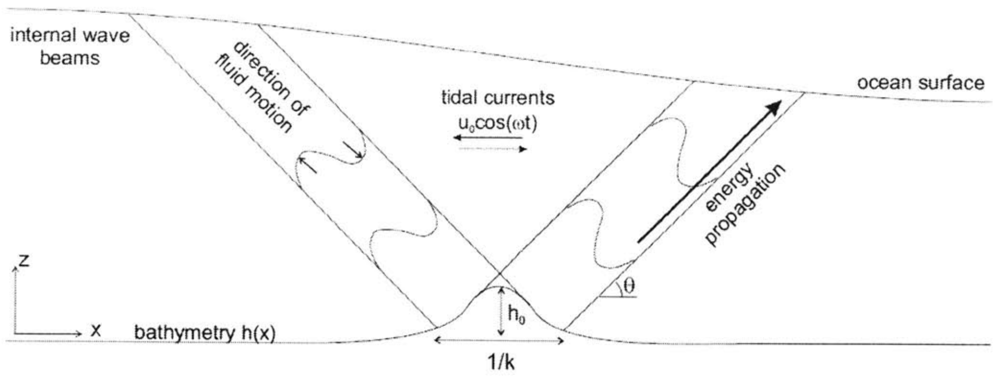

Figure 1-1: Schematic of internal tide generation in the deep ocean.

the barotropic tides over the steep Hawaiian ridge and found a $9.7G\,\mathrm{W}$ energy flux in the form of an internal wave of tidal frequency, also referred to as an internal tide.

Most of the energy in the wave beam that propagates away from topography is in the first spatial mode that corresponds to the horizontal scale of the topography. The subsequent dissipation of internal tides in the ocean is not yet fully understood, but it is established that overturning and mixing are most likely to occur for beams with higher wave numbers, as explained by St. Laurent and Garret [33], who investigate the spatial distribution of mixing in an internal wave field. Internal waves with higher wave numbers are generated by local nonlinear phenomena over steep bathymetry or else have evolved from low mode waves and therefore occur further from their generation site.

Observations have reported mixing associated with internal waves radiated off steep topography. Ledwell et. at. [?] found high levels of mixing over the rough bathymetry along the mid-Atlantic ridge in the Brazil basin. Lueck and Mudge [23] report mixing locally over the Cobb seamount in the north-eastern Pacific; Rudnick et. al. [32] observed turbulent mixing over the Hawaiian ridge; and Lien and Gregg [20] observed high levels of shear and turbulence along the internal wave beam radiated off the shelf break near Monterey Bay. The transfer of energy to higher modes may take place through different processes, including nonlinear wave-wave interactions such as the parametric subharmonic instability (PSI), which has been simulated numerically by MacKinnon and Winters [24]; and scattering by rough bottom topog-

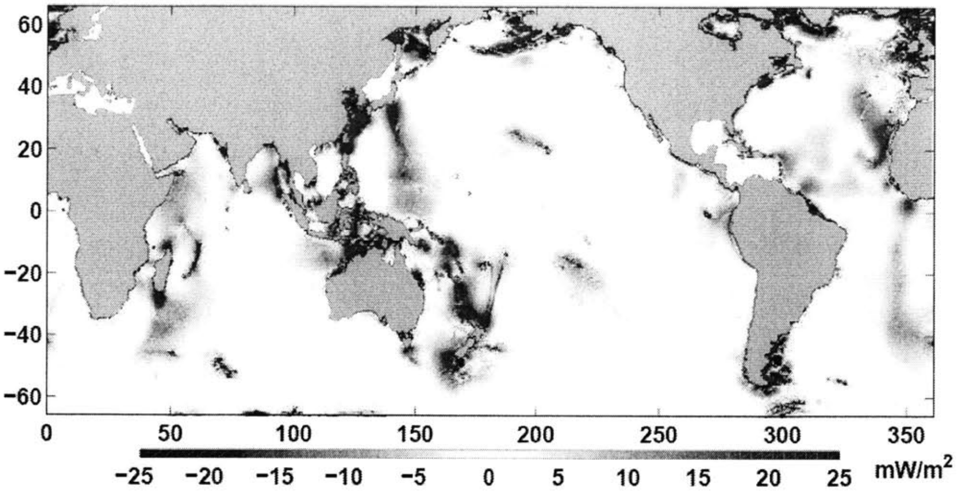

Figure 1-2: Energy loss from the barotropic tide calculated by Egbert and Ray [5] from satellite altimetry data.

raphy, discussed by St. Laurent and Garret [33]. Another process that transfers internal wave energy to higher modes is the reflection of the beams off slopes that coincide with the angle of the beam propagation (critical slope), and Nash et. al. [27] measured high levels of mixing on the critical continental slope off the coast of Virginia. As pointed out by Cacchione et. al. [3], the slope of the continental shelf often coincides with the propagation angle of first mode internal waves, which suggests that these have a role shaping the continental shelf.

Ultimately, the mixing associated with internal tides, which may dissipate as much as the 1 T W of tidal energy loss in the deep ocean, is important because it can help drive ocean circulation. This was first suggested by Munk and Wunsch [26], who estimate that 2.1 T W of power is required to maintain the circulation observed in the deep ocean, and note that only about 1 T W is input by wind action on the ocean surface. This argument has been reviewed by Wunsch and Ferrari [40], who argue that the spatial distribution and magnitude of the dissipation of internal tides should be included in ocean circulation models. The oceanographic interest in this topic has motivated much research, including projects such as the Hawaii Ocean-Mixing Experiment (HOME), which aims to bring together theory with numerical and field observations of the energy cascade from tides to turbulent mixing off the Hawaiian ridge [13].

1.2 Studies of tidal conversion by two-dimensional topography

The observations made by Egbert and Ray [5] motivated analytical studies focused on modelling internal tide generation at primarily two-dimensional (2D), idealized topographies and estimating linear tidal conversion rates. Further numerical studies test these predictions and expand the investigation into nonlinear regimes. There is an emphasis on 2D topographies because these are the strongest generator of internal tides in the ocean: as pointed out by Holloway and Merrifield [12], tidal currents can flow around 3D mounts but not around long ridges, in which case the barotropic currents are forced to displace vertically and generate baroclinic disturbances.

Four non-dimensional parameters that characterize 2D internal tide generation. They are introduced here following the nomenclature of Garrett and Kunze [9]. The first two parameters relate the relevant time scales in the system: ω/f relates the tidal frequency ω to the Coriolis frequency f, and ω/N relates ω to the Brunt-Väisälä or buoyancy frequency N, which describes the vertical stratification:

$$N(z)^2 = -\frac{g}{\rho_*}\frac{\partial\rho(z)}{\partial z}. \tag{1.1}$$

Here, z is the vertical coordinate, $\rho(z)$ is the local density, g is the gravitational acceleration and ρ_* is a constant reference density value that can be taken to represent the local density in a Boussinesq fluid. These parameters govern the angle θ of propagation of the wave beams via the dispersion relation for small amplitude, 2D internal waves:

$$\alpha = \tan\theta = \sqrt{\frac{\omega^2 - f^2}{N^2 - \omega^2}}, \tag{1.2}$$

such that wave beams only propagate if $f < \omega < N$.

The other two parameters relate relevant spatial scales: the criticality parameter $\varepsilon = h'_{\max}/\alpha$ is the ratio of the maximum slope $h'_{\max}$ of bottom topography described by $z = h(x)$, to the slope of the radiated wave beam $\alpha = k/m = \tan\theta$; and the tidal excursion parameter ku_0/ω, which is the ratio of the tidal displacement $A = u_0/\omega$, where u_0 is the maximum velocity of the tides, to the horizontal scale of the topography k^{-1}. The tidal currents, the dimensions of the topography and the angle of propagation of internal wave beams are indicated in figure 1-1.

The early analytical results of Bell [2] considered tidal conversion by weak topography ($\varepsilon \ll 1$) with arbitrary excursion in a fluid of infinite depth. Under the weak topography assumption the bottom boundary condition can be linearized and applied at $z = 0$ rather than at $z = h(x)$; the solution is then found using Fourier analysis. Bell's work has been extended to other parameter regimes by a number of researchers, including Llewellyn Smith and Young [21], who solved the problem for weak topography and short tidal excursion ($ku_0/\omega \ll 1$) in finite-depth and varying stratification. For short tidal excursion the equations can be linearized about hydrostatic equilibrium by neglecting advective terms. Another relevant solution is that of Balmforth, Ierley and Young [1], who account for finite-slope, subcritical topography ($\varepsilon < 1$) and assume $ku_0/\omega \ll 1$ in infinite depth.

The case of strongly supercritical topography has also been investigated analytically using linearized equations, with the canonical configuration being a knife-edge. St. Laurent et. al. [34] obtained a matrix problem for a knife-edge, a step or a top-hat ridge by matching boundary conditions, then found the modal solutions numerically; and Llewellyn Smith and Young found an analytic expression for the energy flux radiated from a knife-edge [22]. Recently, Petrelis, Smith and Young [30] used a Green's function approach to find a solution for a triangular ridge that spans subcritical to supercritical parameter regimes. These solutions were obtained for finite-depth boundary conditions. The work of Hurley and Keady [15] on oscillating elliptical cylinders can also be adapted to account for the wave field generated by an oscillating knife-edge in a fluid of infinite depth.

Numerical estimates of tidal conversion rates by idealized, 2D topographies were obtained by Khatiwala [16]. These have served as a preliminary test of linear models of subcritical generation. Khatiwala did a non-hydrostatic and nonlinear numerical simulation using the MIT General Circulation Model (GCM) to test the effects of finite depth on estimates of energy flux at Gaussian and sinusoidal subcritical topographies. In doing so, he extended his investigations to consider the transition into supercritical regimes. For a critical Gaussian ridge he predicted a $10 - 20\%$ increase in energy flux with respect to estimates using Bell's model for weak topography. This is in agreement with estimates by Balmforth, Ierley and Young [1], who predict that the energy flux from a critical Gaussian ridge is 14% greater than predicted using Bell's model.

Overall, estimates from linear analytical models, numerical simulations and measurements of ocean altimetry are in reasonable agreement and suggest a high level understanding of energy conversion rates by 2D topography in the deep ocean. For instance, linear models have been used to make estimates of the total tidal conversion by bathymetry that are comparable to the corresponding values suggested by Egbert and Ray [5]. St. Laurent and Garret [33] do a perturbation expansion to the expression for energy flux obtained using Bell's model. They estimate $3.8 \pm 1.7G\,\mathrm{W}$ of energy flux over $10^6\,\mathrm{km}^2$ of rough bathymetry in a region of the mid-Atlantic ridge. Llewellyn Smith and Young [21] use their finite-depth model to estimate $0.25G\,\mathrm{W}$ in an area of the same size made up of seamounts of 1.6 km radius and 0.32 km high, chosen from statistical samples to represent be representative of the ocean floor. After extrapolating for the extension of the ocean floor, which is about $361 \times 10^6\,\mathrm{km}^2$, these estimates are within an order of magnitude of the world wide conversion rate of 1 T W that Egbert and Ray estimate as unaccounted for by bottom friction [5].

There has also been reasonable agreement in the estimates of tidal conversion rates at supercritical topography. For example, by modelling the Hawaiian ridge as a knife-edge, St. Laurent et. al. [34] estimate that it converts energy at a rate of $21G\,\mathrm{W}$. This is close to $20G\,\mathrm{W}$ of estimated tidal dissipation obtained by Egbert and Ray [5] from the ocean surface elevation at the site; and also comparable to $9.7G\,\mathrm{W}$, which is the numerical prediction of the energy flux away from the Hawaiian ridge by Merrifield and Holloway [25].

This agreement supports the use of linear models to estimate tidal conversion rates, which are integral quantities; but there is no consistent understanding throughout the different studies of the structure of the wave field, in particular as ε and ku_0/ω increase. For instance, Balmforth, Ierley and Young [1] observe that, for generation problems with large subcritical ε and strong forcing, their linear solution shows reversals in the vertical stratification along radiated wave beams, which Petrelis et. al. [30] also note in their linear solution to supercritical generation. These buoyancy instabilities hypothetically allow overturning and mixing. The numerical experiments performed by Khatiwala for the same large, subcritical ε show high local velocities that would break down linear theory and result in strong shear, but there is no evidence of overturning in the region. As mentioned above, there is evidence from field observations of mixing near sites of supercritical generation, although the mechanisms at work have not been identified. The presence of instabilities in the wave field and the onset of overturning is yet to be understood.

A more accurate account of the presence of instabilities could help improve predictions of mixing and dissipation, and how these affect ocean structure and circulation. The previous discussion suggests that linear solutions for topography with finite and even large slopes are not good enough to describe the local wave field or to predict the onset of overturning and mixing. Numerical and field experiments may provide further insight, but they are hindered by limited resolution. A series of laboratory experiments would therefore be a good approach.

To date, there have been no controlled and quantitative laboratory experiments to test any of the predictions made using linear analytical models. These experiments would be useful to corroborate the local structure predicted by the linear models and to investigate the mechanisms that smoothen the singularities found in the linear wave field solutions in nonlinear regimes.

1.3 Overview of the experimental investigation

The goal of this work is to perform a quantitative experimental study to test the predictions of existing linear, analytical models of internal tides generation by idealized, 2D topography. The experimental wave fields were obtained using a novel optical technique called synthetic Schlieren (SS) [35]. These were compared to the analytical wave fields predicted by Balmforth, Ierley and Young [1] for a finite-slope, subcritical Gaussian ridge, and of Hurley and Keady [15] for a strongly supercritical knife-edge ridge. To warrant the comparison with experimental data in which the effect of dissipation was manifest, we modified Balmforth's analytical model to account for weak viscosity; this was already accounted for by Hurley and Keady [15].

For practical reasons we chose to simulate internal tide generation at 2D topographies in the absence of background rotation. This is a relevant scenario because 2D topographies are strong generators: for instance, St. Laurent et. al. [34] use a 2D model to estimate tidal conversion at the Hawaiian ridge, and this is within $O(5\%)$ of the tidal conversion estimates from observations. Furthermore, the SS technique has been proven to give accurate quantitative data for nominally

2D wave fields [35]. The effect of removing background rotation is an increase in the energy flux: Bell's theory for a Gaussian ridge suggests a 15% increase in this case.

Chapter 2 is an overview of the experimental arrangement and the SS technique. Chapter 3 introduces the general analytic problem for linear internal wave generation, and chapters 4 and 5 present the solutions to this problem and accompanying experimental results for the Gaussian and the knife-edge ridges, respectively. Chapter 6 is a discussion of the comparisons between experimental results and linear analytical solutions, as well as a discussion of experiments outside of linear generation regimes, for which we seek evidence of instabilities and flow separation. Finally, chapter 7 presents conclusions and suggests future experimental studies of internal tides.

Chapter 2

Experimental Arrangement

2.1 Generation of internal tides

Internal tides are generated by side to side currents flowing over topographic features. In the laboratory, we simulated internal tide generation in the frame of reference of tidal currents, by moving a topographic feature from side to side inside a tank filled with salt-stratified water.

The experiments were performed in a 1.32 m-long, 0.2 m-wide and 0.66 m-high tank with 20 mm-thick Plexiglas walls; illustrated in figures 2-1 and 2-2. A support frame of 80/20 beams was placed surrounding the tank and used to mount two motion controlled traverses. One of these was used to drive the topography motion and the other was used to hold a PME conductivity and temperature (CT) probe. Both the tank and the support frame were clamped to a lab bench and levelled to within 0.04 ° with the horizontal as measured using a Starrett spirit level.

An UHMW polyethylene sliding stage, shown in figure 2-3, was placed on the base of the tank and also levelled to within 0.04 ° with the horizontal. One side of the stage was connected through a pulley to a spring mounted on the support frame, and the other side was similarly connected to a traverse driven by a Lintech stepper motor, as illustrated in figure 2-1. The 2D topographic features used to generate the wave field were flush-mounted to the moving surface of the stage. One of the topographic features was a Gaussian ridge, cut out of insulating foam using a CNC foam-cutter, that was $h_0 = 14.7 \pm 0.2$ mm-tall and had a standard deviation of $\sigma = 20$ mm, which is shown on the stage in figure 2-3. The other topography was a

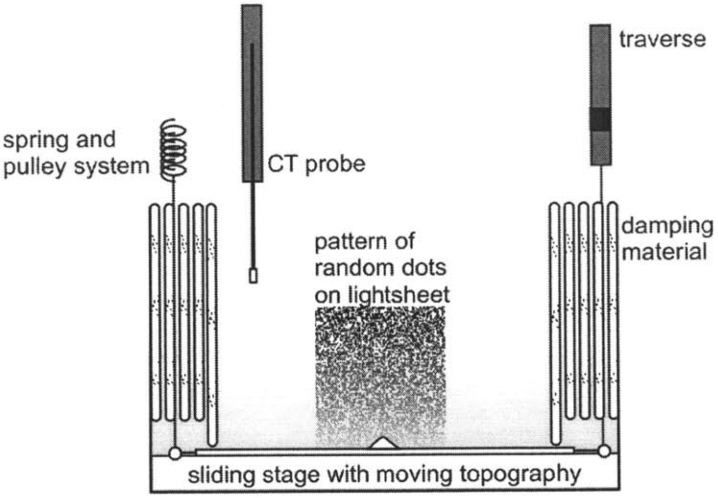

Figure 2-1: Schematic of the experimental tank

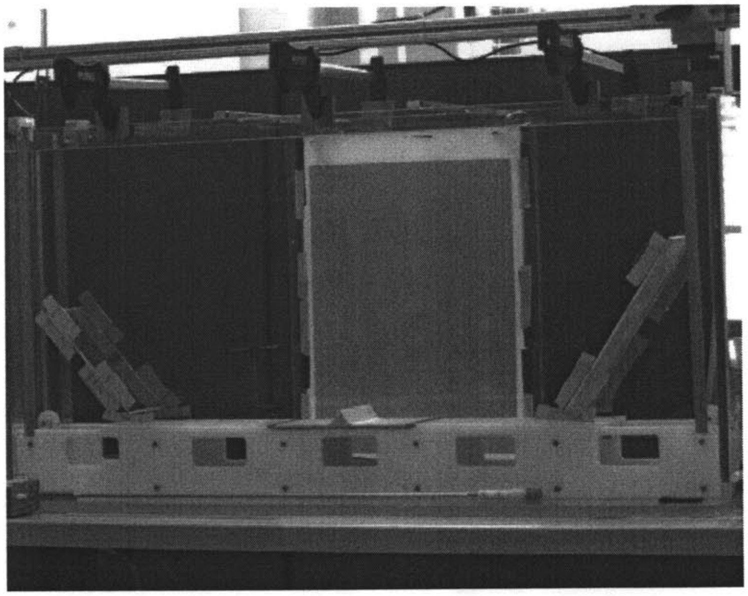

Figure 2-2: Photograph of the experimental tank

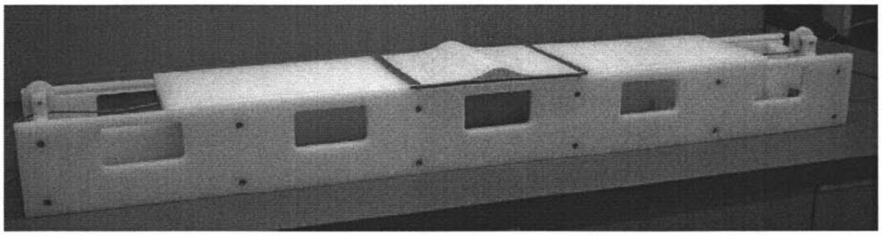

Figure 2-3: Photograph of the sliding stage with a Gaussian topography

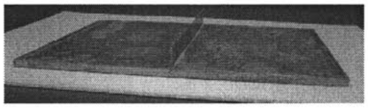

Figure 2-4: Photograph of the knife-edge

16.0 ± 0.2 mm-tall and 1.0 ± 0.2 mm-thick knife-edge, machined out of stainless steel, shown in figure 2-4.

The side walls of the tank were lined with Blockson filter material, a coarse coconut-hair matting, as shown in figure 2-1. The matting trapped the wave beams generated by the edge of the moving surface and the pulleys, preventing them to enter the field of view. It also damped the wave beams reflected from the end walls. Figure 2-5 shows a beam reflected off the matting that decreases 70% amplitude.

The topography mounted on the sliding stage followed a sinusoidal trajectory in the horizontal plane. This was specified using LabVIEW and commanded to the traverse via a NI PCI-7344 motion control card and an API Controls P261 micro-stepper drive. The setup was used to generate smooth sinusoidal trajectories with excursion amplitudes A between 0.9 mm and 7 mm, and time periods T_p between 6 s and 12 s. There were slight discrepancies between the commanded and the actual trajectories, possibly due to elasticity in the wire and some stick-slip as the stage slowed down at either end of its oscillation. The true trajectories were measured by capturing the motion of the topography using a JAI CV-M4+CL CCD camera, with a resolution of 1268 by 1024 pixels, and a BitFlow RoadRunner video card. The position of the topography during the movie was tracked using MATLAB. Figure 2-6 shows two

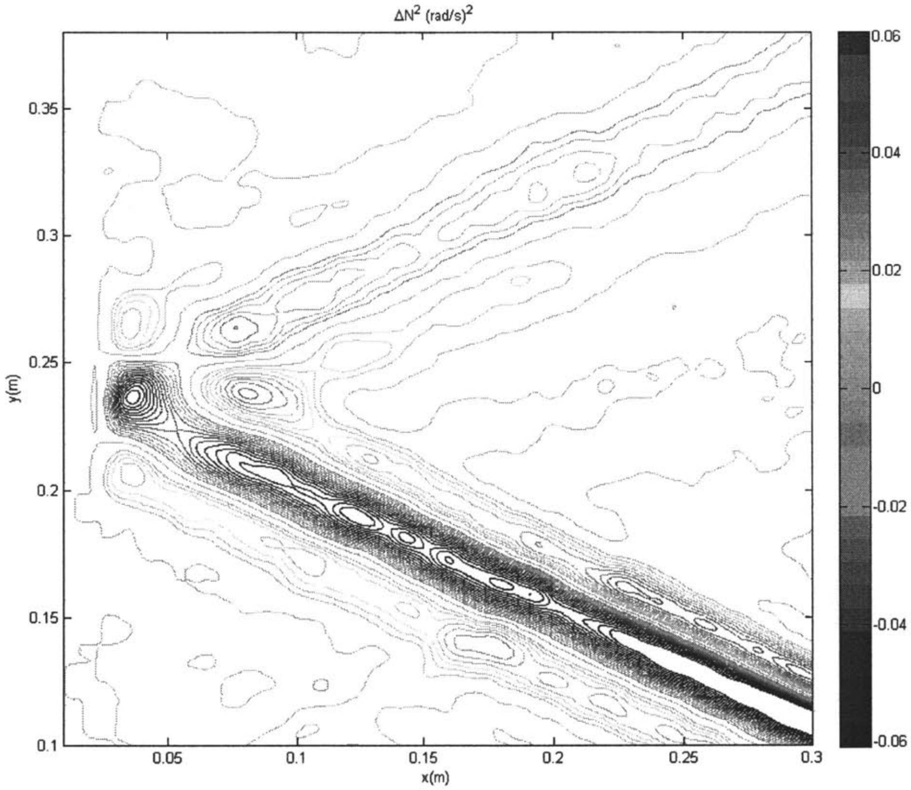

Figure 2-5: Contour plot of the disturbances to the buoyancy frequency by an incident beam and its reflection off coconut matting

sample trajectories where the commanded amplitudes were $A = 3.5\,\text{mm}$ for an oscillation with $T_p = 6.16 \pm 0.04\,\text{s}$ and $A = 1.25\,\text{mm}$ for $T_p = 11.92 \pm 0.04\,\text{s}$. The actual amplitudes achieved were $2.58 \pm 0.05\,\text{mm}$ and $0.90 \pm 0.05\,\text{mm}$, respectively. Note that the sinusoids are slightly flattened when stick-slip was starting to take place, most dramatically for the latter trajectory, which corresponds to the slowest experiment performed. The maximum velocity of the flow over the topography was obtained by fitting a linear slope through the section of the trajectory around the center of the oscillation. This was averaged over 5 to 10 sweeps of the topography in order to get an accurate estimate.

A linear density stratification was established in the experimental (wave) tank using the Oster double-bucket technique [10]. The double-bucket system used, which is shown in figure 2-7, comprised two 90-liter buckets, three pumps and two Omega FTB601 flow meters. The first bucket was filled with salt-water of $1130 \pm 1\,\text{kg/m}^3$ and the second bucket was filled with fresh water. Water from the first bucket was pumped into the second bucket at $0.75 \pm 0.01\,\text{l/min}$, and simultaneously the mixed water was pumped into the bottom of the experimental tank at $1.50 \pm 0.01\,\text{l/min}$, yielding a constant density change. The third pump was used to constantly recirculate the water in the second bucket and keep the mixture homogeneous. Saltier water flowing into the experimental tank displaced the lighter, fresh-water upward, creating a vertical stratification. The tank was filled with 158 liters in 105 min, and the stratification was left to settle for an hour before any experiments were carried out.

The density profile in the experimental tank was measured using the CT probe. The temperature-voltage output was calibrated using an OMEGA HH42 digital thermometer accurate to 0.01 °C. Then, the probe was calibrated to measure density. The conductivity voltage output consists of an amplified voltage across two sensor terminals that, when submerged in a sample of salt-water, is affected by salt concentration and by temperature. Therefore, a calibration surface was plotted by interpolating two curves of density as a function of conductivity at two different temperatures. An example is shown in figure 2-8. This was obtained by measuring the voltage output and the density of two sets of ten salt-water samples between $1000\,\text{kg/m}^3$ and $1100\,\text{kg/m}^3$. The densities were measured using an Anton Paar DMA 38 density meter that is accurate to $0.1\,\text{kg/m}^3$. The first set of samples was kept at $19.0 \pm 0.1\,^\circ\text{C}$ and the second at $24.0 \pm 0.1\,^\circ\text{C}$ using Neslab RTE-140 temperature control units and confirmed

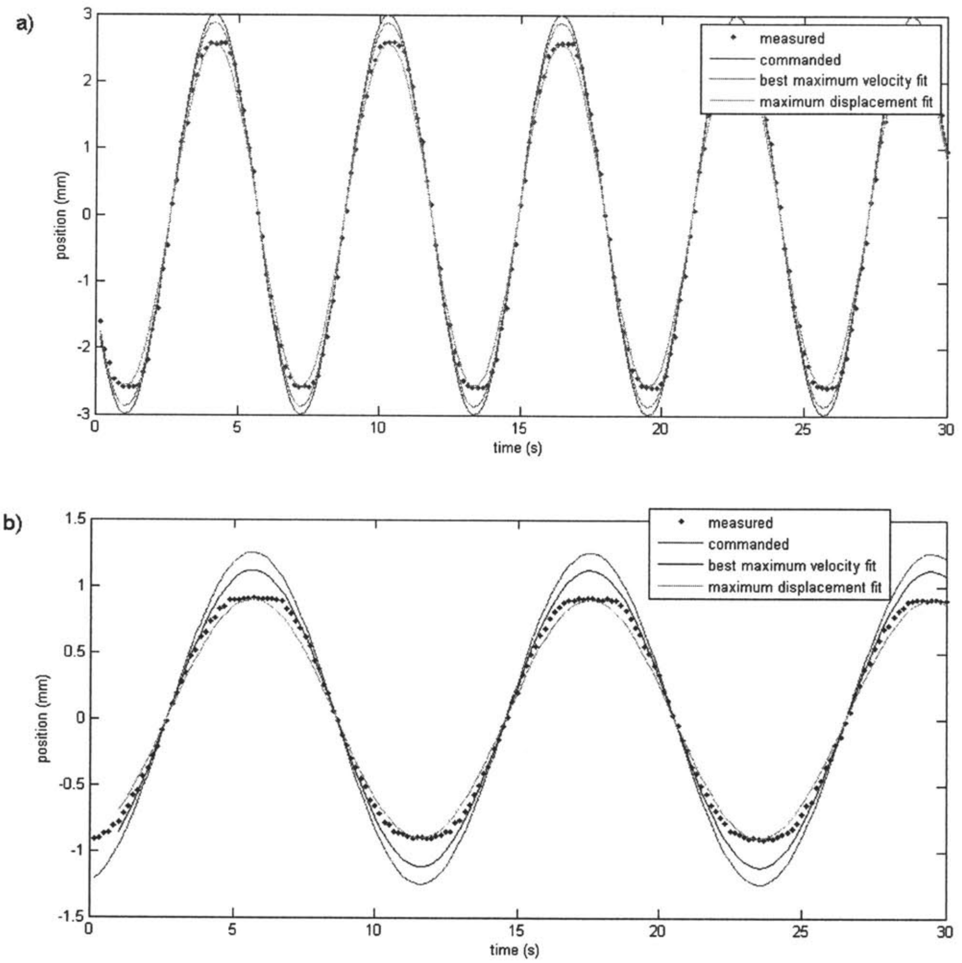

Figure 2-6: Comparison of the commanded versus the measured trajectories of the topography. The sinusoids commanded were to a) $A = 2.58 \pm 0.05\,\mathrm{mm}$ and $T_p = 6.16 \pm 0.04\,\mathrm{s}$; b) $A = 0.90 \pm 0.05\,\mathrm{mm}$ and $T_p = 11.92 \pm 0.04\,\mathrm{s}$.

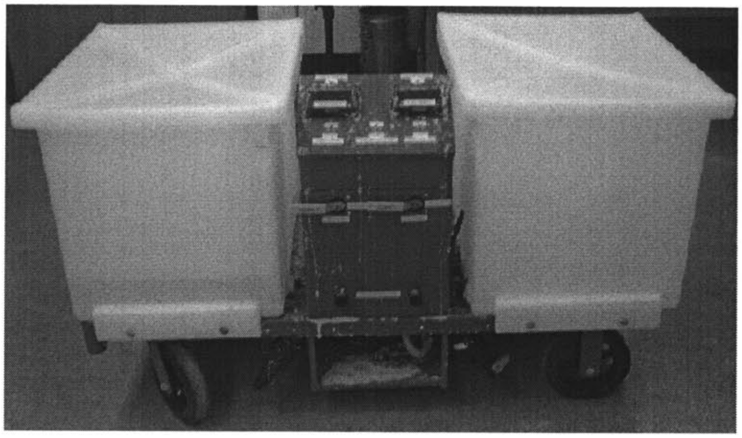

Figure 2-7: Double-bucket system

using the digital thermometer. Thus, the two set of samples spanned the variations in density and temperature found in the tank. The conductivity and temperature-voltage outputs from the probe were connected to a NI BNC-2090 connector block and captured using a NI DAQ PCI-6036E data acquisition card and the NI Measurement and Automation software interface. The accuracy of the density measurements obtained using this technique was approximately $0.5\,\mathrm{kg/m^3}$, corresponding to 0.25% of the working density range. This was confirmed by comparing the density measurements using the probe and the density meter for two test samples at intermediate temperatures.

The calibrated probe was then mounted on a motion-controlled traverse and driven vertically through the tank, while its conductivity and temperature voltage outputs were recorded and translated into a density profile using the calibration surface. The density profile for a typical experiment is shown in figure 2-9, which shows a very constant slope of $-148 \pm 5\,\mathrm{kg/m^4}$. The background density measured 10 cm above the bottom surface was $\rho_* = 1065\,\mathrm{kg/m^3}$, and using this as a reference value, the buoyancy frequency was calculated using the definition in equation (1.1) to be $N = 1.17 \pm 0.02\,\mathrm{rad/s}$. Note that, since the density varies between 1050 and $1080\,\mathrm{kg/m^3}$ in the wave field of interest, this value of the buoyancy frequency can vary about $0.008\,\mathrm{rad/s}$ depending on the choice of ρ_*, which is within the measurement uncertainty.

While we were able to measure the salinity profile using the CT probe, we determined that

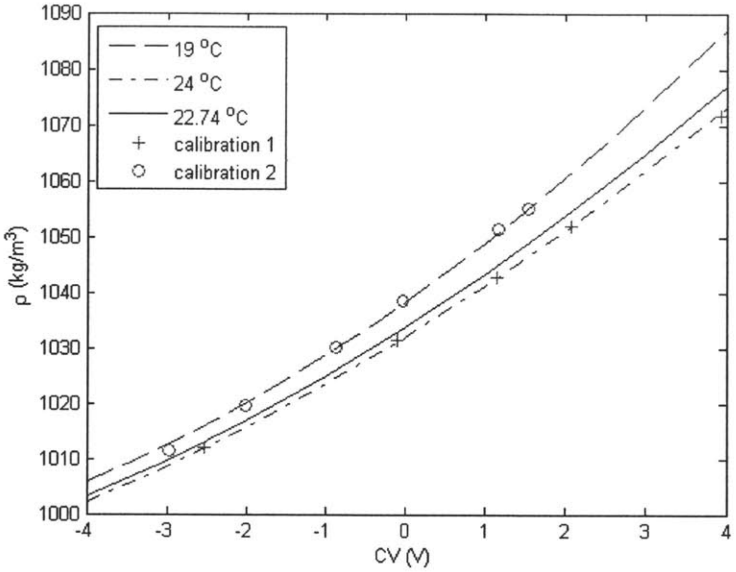

Figure 2-8: Density calibration surface for the CT probe

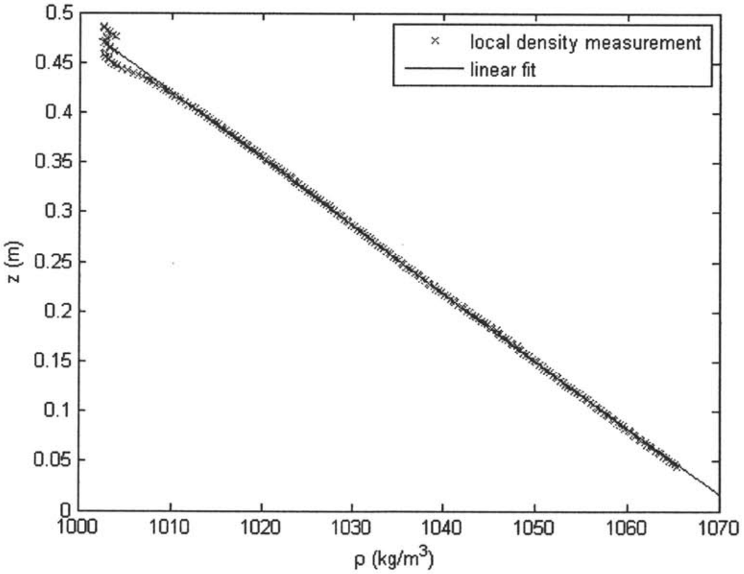

Figure 2-9: Sample density profile

a faster and equally accurate method was to obtain the density profile using the dispersion relation for Boussinesq waves in the absence of background rotation (from equation (1.2) for $f = 0$):

$$\sin\theta = \frac{\omega}{N} \tag{2.1}$$

The forcing frequency ω was known and the beam angle θ was measured from a processed experimental image of a wave beam using the Radon transform in MATLAB, as was done previously by Peacock and Weidman [29]. The Radon transform maps the sum of the intensities in a column of pixels into a single horizontal line. This was used to measure the beam angle by rotating the image by 1 ° increments and noting the angle at which the largest intensity peak was observed, which is when the full length of a bright wave beam collapsed onto one point. Using this method, the value of N measured for the same stratification shown in figure 2-9 was $N = 1.20 \pm 0.02\,\mathrm{rad/s}$, and the linearity of the stratification was evident in the uniformity of the wave beams.

The viscosity coefficient ν for salt water of $1070\,\mathrm{kg/m^3}$ at room temperature of $21\,^\circ\mathrm{C}$ was measured to be $1.10 \pm 0.04 \times 10^{-6}\,\mathrm{m^2/s}$ using a size 75 glass capillary kinematic viscometer. This value varied by $0.04 \times 10^{-6}\,\mathrm{m^2/s}$ over the 1050 to $1080\,\mathrm{kg/m^3}$ range in the region of interest in the wave field. An AR-1000N rheometer was also used to measure the kinematic viscosity of a salt-water sample at $1070\,\mathrm{kg/m^3}$ by placing the sample between two rotating plates and measuring the shear stress. The value of ν measured was $1.10 \pm 0.02 \times 10^{-6}\,\mathrm{m^2/s}$, and this remained constant to within $0.02 \times 10^{-6}\,\mathrm{m^2/s}$ for shear rates from 10 to 1000 Hz.

2.2 Measurement of internal tides: synthetic Schlieren

The wave field was studied using the SS technique developed by Dalziel et. al. [4], which measures the changes in the refractive index of a medium by tracking the apparent distortions of an image viewed through the medium. This principle is used to measure weak perturbations to a density gradient, which have a linear effect on the refractive index gradient of a stratified flow.

The refractive index field $n(x, z)$ in a 2D stratified flow in the vertical plane can be decom-

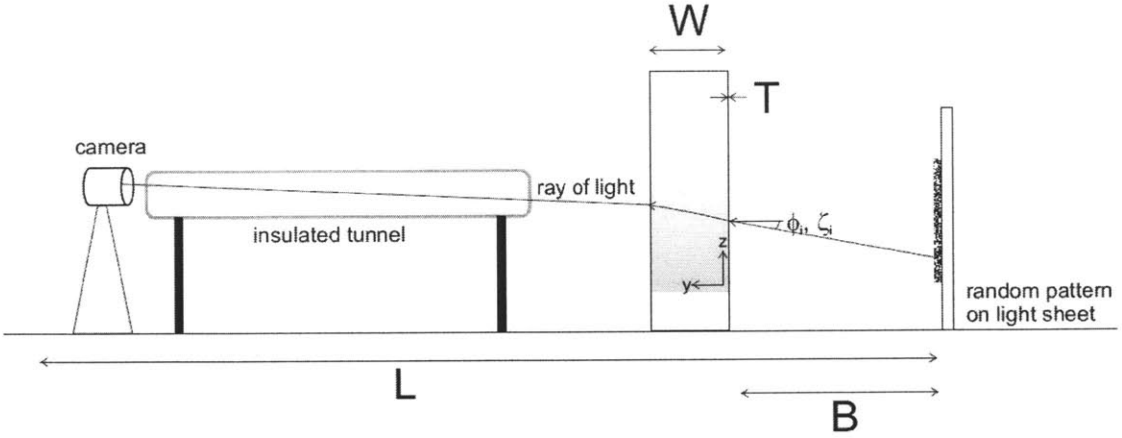

Figure 2-10: Schematic side-view of the synthetic schlieren set up

posed into three terms:

$$n(x,z) = n_w + n_b(z) + n'(x,z), \tag{2.2}$$

where $n_w = 1.33$ is the refractive index of fresh water, n_b corresponds to the increase in the refractive index by the base stratification, and n' is the effect of small amplitude perturbations to the stratification. The relationship between the refractive index and the density gradient can be approximated as

$$\nabla n = \beta (n_w/\rho_w)\nabla\rho, \tag{2.3}$$

where $\rho_w = 1000\,\mathrm{kg/m^3}$ is the density of fresh water and $\beta \approx 0.184$ for salt-water stratifications [39].

Figure 2-10 shows a schematic of the vertical plane in which a light ray described by $\zeta(y,z)$ travels from a light source, through a tank containing a stratification, and towards an observer or a camera. The distance between the back wall of the tank and an image behind it is denoted as B, the inner width of the tank is W, the full distance between the image and the camera in front of the tank is L, and the thickness of the tank walls is T. The path $\zeta(y,z)$ must curve towards the higher refractive index to satisfy Snell's law

$$\delta \int n(y,z)ds = 0, \tag{2.4}$$

where ds is the integration variable along ζ. For light rays that are almost parallel to the y-direction across the tank, the variational principle applied to equation (2.4) yields

$$\frac{d^2\zeta}{dy^2} = \left[1 + \left(\frac{d\zeta}{dy}\right)^2\right] \frac{1}{n}\frac{dn(z)}{dz} \approx \frac{1}{n}\frac{dn(z)}{dz} \tag{2.5}$$

such that

$$\zeta(y,z) = \zeta_i + y\tan\phi_i + \frac{1}{2}y^2 + \frac{1}{n(z)}\frac{\partial n(z)}{\partial z}. \tag{2.6}$$

Here, ζ_i and ϕ_i are the position and angle of incidence of a light ray entering the stratification. The refraction of light causes an apparent displacement of the image viewed through the disturbed medium that can be denoted by $\Delta\zeta$ and that is proportional to the perturbations:

$$\Delta\zeta = -\frac{1}{2}\left(1 - \frac{W+2B}{2L}\right) W \left(W + 2\frac{n_w}{n_{air}}B + 2\frac{n_w}{n_{wall}}T\right)\beta\frac{\rho'_z}{\rho_w} \tag{2.7}$$

where $n_{air} = 1$ is the refractive index of air and $n_{wall} = 1.49$ is the refractive index of the acrylic wall.

The experimental arrangement was set up as illustrated in figure 2-10, where the relevant distances were $B = 0.465 \pm 0.001\,\mathrm{m}$, $W = 0.200 \pm 0.002\,\mathrm{m}$, $L \simeq 4.30 \pm 0.05\,\mathrm{m}$ and $T = 0.019\,\mathrm{m}$. The image used was a random pattern comprising dots 0.5 mm in diameter and spaced about 0.5 mm apart, printed on a transparency and put on a 30 by 25 cm Per'f Alite electroluminescent sheet. The apparent distortion of the pattern caused by the wave field was captured at 6 frames per second using the CCD camera. This was placed far from the front of the tank in order to minimize parallax, such that the area imaged subtended an angle of less than 3° and the dots-size was about 4 square pixels.

The intensity variations in the light source introduce noise to the experimental measurement because apparent displacements are measured by tracking the changes in intensity in the movie, as will be explained below. The light sheet intensity was found to be as stable as the intensity of the fluorescent tubes that had been used as a light source in previous SS experiments by

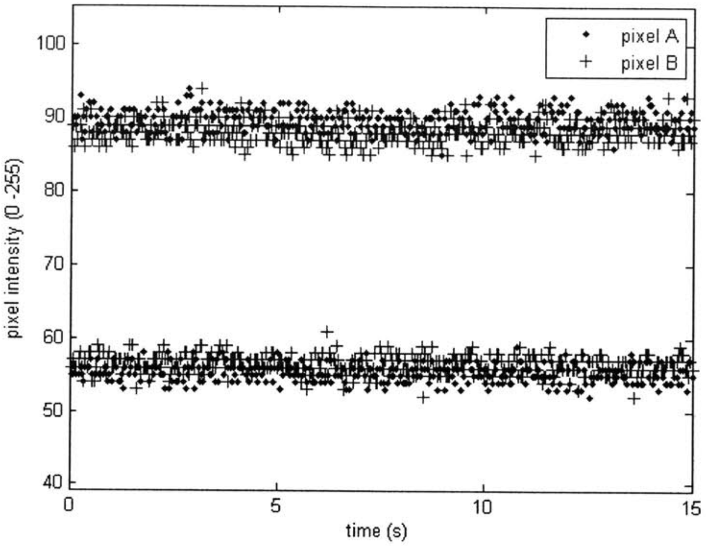

Figure 2-11: Time series of intensity values measured on two different pixels and for two different intensity settings on the light sheet.

Sutherland et. al. [35]. These intensity variations were measured by removing the pattern and placing the CCD camera directly in front of the light sheet. Figure 2-11 shows the time series of the intensity values for two separate pixels on the image of the light sheet and for two different light sheet intensity settings. The time series exhibit peak-to-peak fluctuations in intensity P on the order of 5/255 (the intensity of an 8-bit image can vary between 0/255 in black regions and 255/255 in white regions). These were typical variations throughout the light sheet and no spatial correlations were observed.

The intensity values in the images of the pattern of dots during the experiments varied by about 110/255 between the darkest and the lightest regions of the image. We maximized this contrast range by setting the light sheet intensity to its maximum possible value whilst keeping a small camera aperture $f/5.6$ in order to have a good field of view. By increasing the contrast range we minimized the effect of the light sheet fluctuations on the appearance of the pattern of dots, and thus avoided spurious measurements of its apparent displacement.

Thermal noise was minimized during the experiments by turning off the air conditioning in the laboratory and by placing a 1.5 m-long tunnel with Plexiglas windows and insulated walls immediately in front of the camera. These measures reduced the ambient thermal fluctuations in the room, which change the refractive index between the camera and the experiment, thus curving the light rays and affecting the apparent displacement of the image. In particular, considering equation (2.7), for a fixed distance L between the camera and the image, the method is most sensitive for large B, and therefore more sensitive to noise close to the camera.

To measure the apparent displacement observed, the movies were processed using the software DigiFlow. The displacement of the image changes the intensity distribution of the array of pixels that constitutes each frame in the movie captured with the CCD camera. DigiFlow uses a correlation function over interrogation windows of 19 by 19 pixels in size to track the changes of the intensity distribution over the pixel array . The measurement of apparent displacement using DigiFlow is accurate to ± 0.02 pixels when the whole pattern is traversed across the captured image [4], but the working value of the accuracy for smaller apparent displacements is ± 0.1 pixels.

This is converted to perturbations to the density gradient ρ'_z using equation (2.7) and output over the entire wave field as an image with an intensity map given by

$$P(i,j) = \frac{256}{2}\left(\frac{\rho'_z}{\rho_{water}} \div G\right) + 127, \tag{2.8}$$

where G is a scaling factor chosen such that ρ'_z/ρ_{water} spans the range $[-1 : 1]$. This means that $P(i,j)$ has values between $[0 : 255]$ over the full field and can therefore be mapped onto an 8-bit image. This output can be readily converted to perturbations to the square of the buoyancy frequency $\Delta N^2 = -g\rho'_z/\rho_*$.

The experimental data was also filtered to remove any unaccounted noise, such as vibrations in the tank, remaining ambient drifts and a possible thermal expansion of the pattern. DigiFlow measures the apparent displacement with respect to a reference image when the fluid is at rest, so the reference image used was the average of 12 frames in a 2 s period to reduce high frequency noise. The experiment results presented in Chapters 4 and 5 are the values of ΔN^2 across cross sections of the internal wave beams. The time series of ΔN^2 at every point on the cross sections were passed through a 10^{th}-order low-pass filter with cut-off frequency of 1.88 rad/ s, and through an 8^{th}-order high-pass filter with cut-off frequency of $0.31\,\mathrm{rad/\,s}$. These filters removed disturbances that occur on time scales significantly greater or less than the forcing frequency ω. Finally, the values of $\triangle N^2$ were averaged over four consecutive periods of the internal wave in steady state.

Figure 2-12 shows the apparent displacement due only to these mitigated sources of noise, measured in the experiment in the absence of any flow field. The amplitude of the noise was of the order of 0.01 pixels, which, for a typical experiment with $\rho_* = 1065\,\mathrm{kg/\,m^3}$, $B = 0.465\,\mathrm{m}$, and $L = 4.30\,\mathrm{m}$ would correspond to $\triangle N^2$ of the order of $10^{-4}\,\mathrm{rad^2/\,s^2}$. The amplitude of the disturbance in an internal wave beam in the experiment was roughly $0.04\,\mathrm{rad^2/\,s^2}$, so this noise corresponds to a signal to noise ratio of $O(40)$.

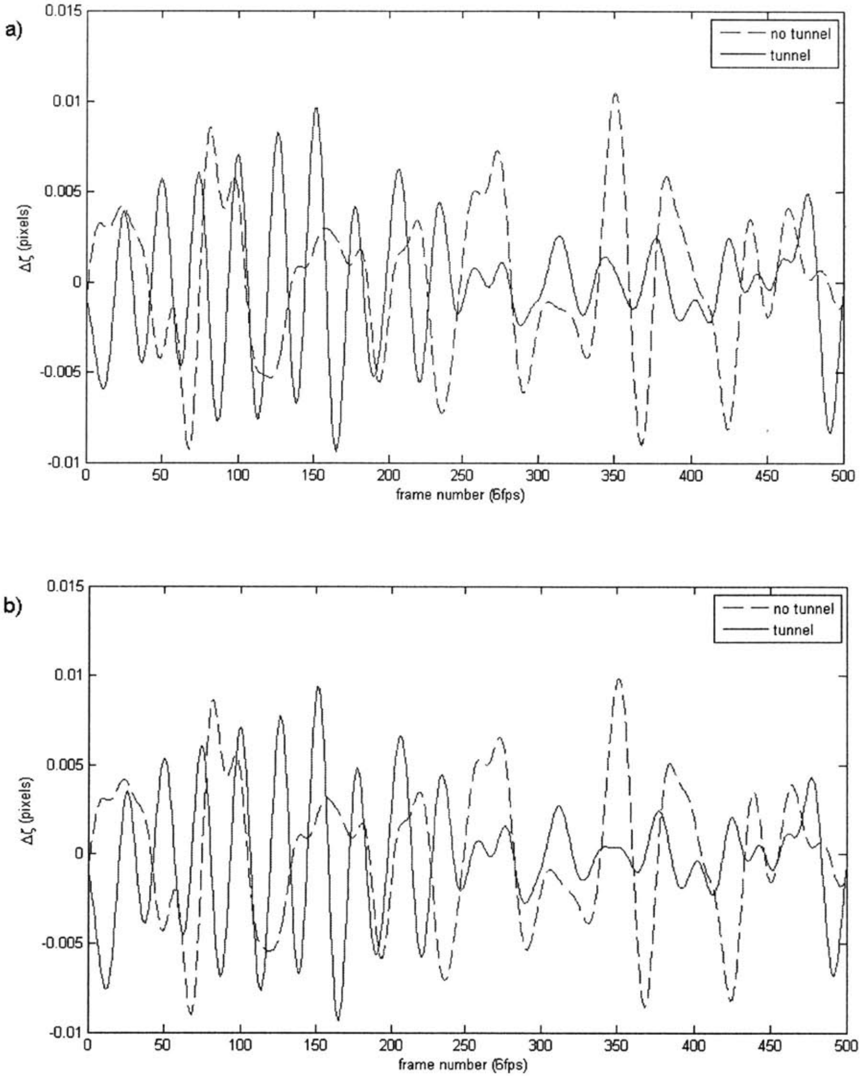

Figure 2-12: Apparent displacement measured in the absence of a wave field in the experimental tank.

Chapter 3

Governing Equations

This chapter presents the form of the Navier-Stokes equations used to model the generation and propagation of internal waves for different configurations in chapters 4 and 5. We follow the discussion in sections 3 to 5 of LeBlond and Mysak [19] to express the Navier-Stokes equations in a rotating frame of reference, linearize them about hydrostatic equilibrium, and express them in an approximately Cartesian space. Viscosity terms are retained to obtain an analytical solution that accounts for the effects of viscosity on the propagating wave beams generated in the experimental tank. The problem is reduced to a single governing equation with boundary conditions for 2D tidal conversion with small excursion in an infinitely deep fluid.

3.1 Linear Navier-Stokes equations for the stratified ocean

The adiabatic Navier-Stokes equations govern the velocity, pressure and density fields $\mathbf{u}(\mathbf{r}, t)$, $p(\mathbf{r}, t)$, and $\rho(\mathbf{r}, t)$ respectively, where $\mathbf{r}$ is a position vector and the flow is specified following an Eulerian approach. In particular, fluid motion in the ocean is specified with respect to the earth, which is a rotating frame of reference.

The unforced and dissipative momentum equation includes a Coriolis term due to the background rotation of the frame of reference:

$$\frac{D\mathbf{u}}{Dt} + 2\boldsymbol{\Omega} \times \mathbf{u} + \frac{\boldsymbol{\nabla} p}{\rho} - \mathbf{g} = \nu \boldsymbol{\nabla}^2 \mathbf{u}, \tag{3.1}$$

where the convective derivative is

$$\frac{D}{Dt} = \frac{\partial}{\partial t} + \mathbf{u} \cdot \boldsymbol{\nabla} \tag{3.2}$$

and $\boldsymbol{\Omega}$ is the angular velocity of the earth ($|\boldsymbol{\Omega}| = 7.29 \times 10^{-5}\,\mathrm{rad/s}$), $\mathbf{g} = -g\hat{\mathbf{z}} = -9.81\,\mathrm{m/s^2}$ is the gravitational acceleration and ν is the viscosity coefficient. The viscous term is usually neglected in descriptions of high Reynolds number fluid motion in the ocean, but it is retained here because viscosity plays an important role in a laboratory setting.

The density equation for an incompressible fluid is

$$\frac{D\rho}{Dt} = \rho_t + \mathbf{u} \cdot \boldsymbol{\nabla}\rho = 0; \tag{3.3}$$

and conservation of mass is

$$\rho_t + \boldsymbol{\nabla}\cdot\rho\mathbf{u} = \frac{D\rho}{Dt} + \rho\boldsymbol{\nabla} \cdot \mathbf{u} = 0, \tag{3.4}$$

which, substituting equation (3.3) for an incompressible fluid, reduces to the continuity equation

$$\nabla \cdot \mathbf{u} = \mathbf{0}. \tag{3.5}$$

Equations (3.1), (3.3) and (3.5) can be linearized about background, simple-harmonic tidal currents with maximum tidal speed u_0 and tidal frequency ω; in a density and pressure-stratified ocean. This is the state $\mathbf{U(t)} = (u_0 \cos\omega t, 0, 0)$, $\rho = \rho_0(z)$ and $p = p_0(x, z, t) = -\rho_0(z)z\mathbf{g} + c_0 x \cos(\omega t)$, where c_0 is some constant. We consider small perturbations $\mathbf{u}'(x, y, z, t)$, $p'(x, y, z, t)$ and $\rho'(x, y, z, t)$ about this equilibrium state and substitute these into the equations (3.1) to (3.5). If the excursion parameter $u_0\omega/k \ll 1$, both parts of the advective term are small compared to the time derivative of the horizontal velocity:

$$\mathbf{u} \cdot \nabla\mathbf{u} = (u_0 + u) \cdot \nabla u \ll u_t. \tag{3.6}$$

Therefore neglecting the products of small quantities yields

$$\begin{aligned} \mathbf{u}_t + 2\boldsymbol{\Omega} \times \mathbf{u} + \frac{\boldsymbol{\nabla} p}{\rho_0} - \frac{\rho \mathbf{g}}{\rho_0} &= \nu \boldsymbol{\nabla}^2 \mathbf{u}, & (3.7) \\ \rho_t + w\rho_{0z} &= 0, & (3.8) \end{aligned}$$

and

$$\nabla \cdot \mathbf{u} = \mathbf{0}; \tag{3.9}$$

where the primes have been dropped. Note that the last term in the momentum equation is now modified by a pre-factor ρ/ρ_0, and it is the only term in which the density perturbation has a first order effect that cannot be neglected. This is called the buoyancy force, which acts as a restoring force responsible for internal waves in density-stratified flows.

3.2 Approximation to a Cartesian frame of reference

The spatial domain of internal waves is small compared to the curvature of the earth. Internal waves are generated in ocean depths $H = O(10^3\,\mathrm{m})$ and their first mode propagates through horizontal scales $L = O(10^5\,\mathrm{m})$, as reported by St. Laurent and Garret [33], with respect to the radius of the earth which is $R = 6.4 \times 10^6\,\mathrm{m}$ [19]. This domain can therefore be approximated as a Cartesians rather than a curvilinear space, which simplifies the manipulation of the governing equations, via a β-plane approximation.

The position vector $\mathbf{r}$ can be expressed in spherical coordinates (λ, ϕ, r), where λ is the longitude angle, ϕ is the latitude angle and r is the distance from the center of the earth. Alternatively, as shown in figure 3-1, $\mathbf{r}$ can be described with local curvilinear coordinates (x, y, z); these are centered at $r = R$ (where R is the radius of the earth), longitude $\lambda = \lambda_0$ and latitude $\phi = \phi_0$; such that $(x, y, z) = (R(\lambda - \lambda_0), R(\phi - \phi_0), r - R)$. These frames of reference rotate with the earth with angular velocity $\boldsymbol{\Omega} = \Omega(0, \cos\phi, \sin\phi)$.\

The linearized equations (3.7) to (3.9) can be expressed in terms of non-dimensional curvilinear coordinates and velocities defined as

$$(x, y, z)' = \left(\frac{x}{L}, \frac{y}{L}, \frac{z}{H}\right) \tag{3.10}$$

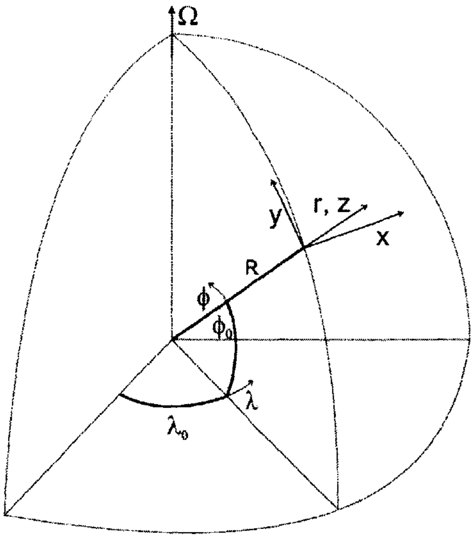

Figure 3-1: Definition of spherical (λ, ϕ, r) and local curvilinear (x, y, z) coordinates on the earth.

and

$$(u, v, w)' = \left(\frac{u}{U}, \frac{v}{U}, \frac{wL}{HU}\right), \tag{3.11}$$

where U is a characteristic horizontal velocity. An initial approximation can be made straight away for local disturbances about latitude ϕ_0 such that $Ly'/R \ll 1$. Under this approximation and using the definitions in (3.10) and (3.11), the momentum equations (3.7) become

$$\begin{aligned}
u_t + 2\Omega\left(-v\left(\sin\phi_0 + \frac{y}{R}\cos\phi_0\right) + w\cos\phi_0\right) + \frac{1}{\rho_0(1 - z'H/R)}\frac{\partial p}{\partial x} &= \nu u_{xx}, & (3.12)\\
v_t + 2\Omega u\left(\sin\phi_0 + \frac{y}{R}\cos\phi_0\right) + \frac{1}{\rho_0(1 - z'H/R)}\frac{\partial p}{\partial y} &= \nu v_{yy}, & (3.13)\\
w_t - 2\Omega u\cos\phi_0 + \frac{1}{\rho_0}\frac{\partial p}{\partial z} + \frac{\rho g}{\rho_0} &= \nu w_{zz}; & (3.14)
\end{aligned}$$

the density equation (3.8) remains unchanged, and the continuity equation (3.9) becomes

$$u_x + \left[v_y + \left(1 + \frac{H}{R}z\right)w_z\right]\left(1 - \tan\phi_0\frac{L}{R}y\right) - v\tan\phi_0\frac{L}{R} + 2w\frac{H}{R}\left(1 - \tan\phi_0\frac{L}{R}y\right) = 0. \tag{3.15}$$

In order to use the β-plane approximation we assume that the horizontal domain of the flow is less than the radius of the earth such that

$$\left(\frac{L}{R}\right)^2 \ll 1; \tag{3.16}$$

also that the ocean is a thin layer of fluid around the earth

$$\frac{H}{R} \ll 1; \tag{3.17}$$

and finally that the fluid motion takes place at low enough latitudes so

$$\frac{L \tan \phi_0}{R} \ll 1. \tag{3.18}$$

Neglecting small terms under assumptions (3.16) to (3.18), the pressure term in the momentum equations (3.12) readily simplifies back to the form $\rho_0^{-1}(p_x, p_y, p_z)$ and the continuity equation simplifies to

$$u_x + v_y + w_z = 0. \tag{3.19}$$

Furthermore, by the same approximation, a line element in space that can be expressed as

$$ds^2 = r^2 \cos^2 \phi d\lambda^2 + r^2 d\phi^2 + dr^2 \tag{3.20}$$

simplifies to

$$ds^2 \approx dx^2 + dy^2 + dz^2. \tag{3.21}$$

This means that the space (x, y, z) behaves as a Cartesian space. Overall, the approximate equations remain in the form of equations (3.7) through (3.9) stated with respect to coordinates (x, y, z), which can be treated as Cartesian coordinates.

Finally, the f-plane approximation can be made. The background rotation of the earth is approximately

$$\boldsymbol{\Omega} \approx (0, \tilde{f}, f + \beta y), \tag{3.22}$$

where

$$\tilde{f} = 2\Omega\cos\phi_0,\ f = 2\Omega\sin\phi_0 \text{ and } \beta = 2\Omega\cos\phi_0/R. \tag{3.23}$$

Assuming that $L\cos\phi_0/R \ll 1$, the vertical component of the background rotation is approximately constant and we can neglect βy, which gives the f-plane equations. Furthermore, if the projection of the depth is small with respect to the horizontal scale of the motion

$$\frac{H}{\tan\phi_0} \ll L,$$

and if the thickness of the fluid layer is small with respect to horizontal scale of the motion

$$\frac{H}{L} \ll \frac{L}{R}; \tag{3.24}$$

then the horizontal component $\tilde{f}$ can be neglected. The momentum equation (3.7) thus simplifies to

$$\mathbf{u}_t + f(-v, u, 0) + \frac{\nabla p}{\rho_0} - \mathbf{g}\frac{\rho}{\rho_0} = \nu\nabla^2\mathbf{u}. \tag{3.25}$$

3.3 Governing equation for linear internal waves in 2D

Equations (3.8), (3.9) and (3.25) can be used to model internal waves generated in the ocean or in a laboratory setting.

To study internal waves it is convenient to express the density field in terms of the buoyancy frequency N given by equation (1.1), which is proportional to the squared root of the background stratification. Furthermore, if the flow satisfies the Boussinesq condition that the variations in density are small over a characteristic vertical distance, namely $\Delta\rho/\rho_0(z) \simeq N^2H/g \ll 1$, then a constant reference value of density can be used throughout the vertical domain: $\rho_0(z) = \rho_*$. The density field in a 2D, Boussinesq flow is therefore composed of three terms:

$$\rho(x, z, t) = \rho_*\left(1 - \frac{N^2 z}{g} - \frac{b}{g}\right), \tag{3.26}$$

where $b(x, z, t)$ is the perturbation to the buoyancy field from the background stratification. In the experiments described in the following sections, the background stratification was constant with buoyancy frequency $N \simeq 1.18\,\mathrm{rad/s}$, and the depth of the water above the bottom of the topography was $H \simeq 0.5\,\mathrm{m}$; so the Boussinesq parameter was $N^2H/g = O(10^{-1})$.

Using expression (3.26), equations (3.8), (3.9) and (3.25) for perturbations about background tidal currents with small excursion in a Boussinesq flow become

$$\begin{aligned} u_t - fv + p_x &= \nu\nabla^2 u, && (3.27)\\ v_t + fu + p_y &= \nu\nabla^2 v, && (3.28)\\ w_t - b + p_z &= \nu\nabla^2 w, && (3.29)\\ b_t + N^2 w &= 0, && (3.30)\\ u_x + w_z &= 0. && (3.31) \end{aligned}$$

To describe the experimental flow, which is 2D and has no background rotation, we neglect any motion across the width of the tank and set the velocity component $v = 0$ and the rotation $f = 0$ respectively. The equations therefore reduce to

$$\begin{aligned} u_t + p_x &= \nu\nabla^2 u, && (3.32)\\ w_t - b + p_z &= \nu\nabla^2 w, && (3.33)\\ b_t + N^2 w &= 0, && (3.34)\\ u_x + w_z &= 0. && (3.35) \end{aligned}$$

The harmonic time-dependence of the tidal forcing $\mathbf{U}(t) = (u_0 \cos\omega t, 0)$ allows us to simplify equations (3.32) through (3.35) by supporting the use of a streamfunction

$$\Psi(x,z,t) = \mathrm{Re}\left[\psi(x,z)e^{-i\omega t}\right], \qquad (3.36)$$

such that $\boldsymbol{u}(x,z,t) = \mathrm{Re}[(-\psi_z(x,z), \psi_x(x,z))e^{-i\omega t}]$. The continuity equation (3.35) is satisfied immediately, and equations (3.32) to (3.34) become a single partial differential equation for ψ:

$$\omega^2\nabla^2\psi(x,z) - N^2\psi_{xx}(x,z) = i\omega\nu\nabla^4\psi(x,z). \qquad (3.37)$$

3.4 Boundary conditions

We solve equation (3.37) for internal wave beams propagating from topography in a semi-infinite domain, constrained only by the bottom boundary, where the solution must also satisfy the radiation condition.

Previous solutions for tidal conversion in the ocean satisfy the inviscid equations and the inviscid bottom boundary condition, including the solutions by Bell [2] and Balmforth, Ierley and Young [1]. In the case of the experiment, for which the flow is weakly viscous, a thin Stokes' boundary layer develops over the surface of the topography. The viscous boundary condition that there is no-slip between the flow and the surface is satisfied by the Stokes' layer, so weakly viscous generation can be approximated by solving the inviscid generation problem. This is done by Hurley and Keady [15], who quote Rosenhead [31] for a discussion of the boundary condition in the presence of a Stokes' layer. The thickness of the Stokes' layer in the experiment is $(2\nu/\omega)^{1/2} \approx O(10^{-3})\,\mathrm{m}$, where $\omega \simeq 1\,\mathrm{rad/s}$ and $\nu \simeq 1.1 \times 10^{-6}\,\mathrm{m}^2/\mathrm{s}$.

Inviscid generation is governed by equation (3.37) for $\nu = 0$ together with the inviscid, no-normal flow boundary condition:

$$[\mathbf{U}(t)+\boldsymbol{u}(x, h(x), t)] \cdot \nabla h(x) = 0, \tag{3.38}$$

which implies that the streamlines of the flow must follow the shape of the topography:

$$\psi(x, h(x)) = u_0 h(x). \tag{3.39}$$

The solution must then be corrected to satisfy the viscous problem in the far field (given by equation (3.37) when $\nu \neq 0$), since the Reynolds number is not large in the experiments; therefore the viscous term affects the propagating beams. Typically for the experiments $Re = u_0/k\nu$ is only $O(10)$, where $u_0 = \omega A = 0.01\,\mathrm{m/s}$ and $k = 1/0.08\,\mathrm{m}^{-1}$.

In the following chapters, equations (3.37) and (3.39) are simplified further so that the inviscid boundary value problem can be solved in the context of the specific form of the bottom topography for a subcritical Gaussian ridge and a knife-edge ridge. The solutions are corrected for weak viscosity by assuming a linear dependence in the direction of the propagation of the waves that satisfies the viscous equation (3.37).

Chapter 4

Generation at a Gaussian ridge

Topography is often idealized as a Gaussian ridge to study subcritical generation of internal waves. Experiments were performed using a Gaussian ridge to compare to the theoretical model of Balmforth, Ierley and Young [1]; one experiment simulated subcritical generation and another simulated near-critical generation, thus spanning the regime in which the model is valid. The analytical solution for comparison with experiments was corrected to account for the effects of viscosity in the propagating beams, following the discussion in section 3.2.

4.1 Analytical solution

The approach of Balmforth, Ierley and Young [1] consists on using Fourier series to solve governing equation (3.37) for flows that are periodic in the horizontal direction, which would occur over topography that is also periodic in x. For instance, consider the periodic topography shown in figure 4-1, which is given by the function

$$h(x) = h_0 e^{-\gamma(1-\cos\kappa x)}. \tag{4.1}$$

where $\gamma = 1/\kappa^2\sigma^2$ and $\kappa^{-1}$and σ have units of length. If γ is large, the height of the topography is significant only near $x = 0, \pi$, in which case $1 - \cos\kappa x \approx \kappa^2 x^2$. In this case the expression in (4.1) describes a series of Gaussian ridges of the form $h_0 e^{-x^2/2\sigma^2}$ for which κ^{-1} indicates the spacing between ridges and 4σ indicates the horizontal scale of each feature.

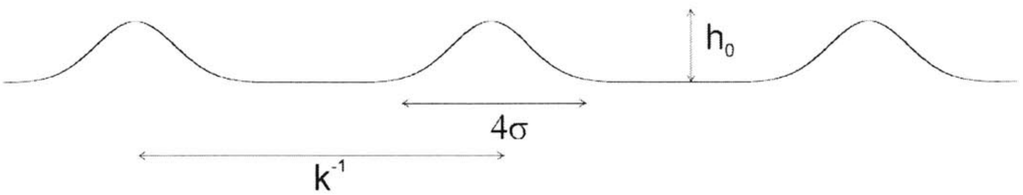

Figure 4-1: Periodic topography with isolated Gaussian ridges $h(x) = h_0 e^{-\gamma(1-\cos\kappa x)}$, where $\gamma = 1/\kappa^2\sigma^2$.

The inviscid generation problem is solved first to find the wave field

$$\psi(x,z) = \sum_{n=-\infty}^{\infty} \psi_n(z) e^{in\kappa x}. \tag{4.2}$$

A second-order ODE for $\psi_n(z)$ is found by substituting ψ from equation (4.2) into equation (3.37) with $\nu = 0$:

$$\omega^2 \left[\psi_n'' - (n\kappa)^2\psi_n\right] + N^2(n\kappa)^2\psi_n = 0; \tag{4.3}$$

which has solutions

$$\psi_n(z) = A_n e^{-ink\mu z} + B_n e^{ink\mu z}, \tag{4.4}$$

where $\mu = \sqrt{N^2-\omega^2}/\omega$. The radiation condition is enforced by keeping only the term in equation (4.4) with values of n for which the exponent is always negative and the beams propagate away from the topography. The inviscid bottom boundary condition given by equation (3.39) is then enforced to determine the modal amplitudes A_n, via

$$\sum_{n=-\infty}^{\infty} A_n e^{-i|n|k\mu h(x)} e^{in\kappa x} = u_0 h(x). \tag{4.5}$$

Equation (4.5) is converted to a linear problem to solve for A_n. First, the summation in

(4.5) is simplified for symmetric topography $h(x) = h(-x)$, which implies that

$$\sum_{n=-\infty}^{\infty} A_n e^{-i|n|k\mu h(x)} e^{in\kappa x} = \sum_{n=-\infty}^{\infty} A_n e^{-i|n|k\mu h(x)} e^{-in\kappa x}. \tag{4.6}$$

We can define $p = -n$ and substitute this into the right hand side of equation (4.6) such that

$$\sum_{n=-\infty}^{\infty} A_n e^{-i|n|k\mu h(x)} e^{-in\kappa x} = \sum_{p=-\infty}^{\infty} A_{-p} e^{-i|p|k\mu h(x)} e^{-ip\kappa x}. \tag{4.7}$$

Since the exponents in both of these summations are the same, then the corresponding coefficients must also be equal, thus $A_n = A_{-n}$. Furthermore, by summing from $-\infty$ to ∞ the odd part of $e^{in\kappa x}$ cancels out, so the series becomes

$$A_0 + 2 \sum_{n=1}^{N\to\infty} A_n e^{-i|n|k\mu h(x)} \cos n\kappa x. \tag{4.8}$$

Now equation (4.5) can be put in the form of an invertible matrix equation $\mathrm{M}_{nl} A_n = \mathrm{B}_l$ by retaining a finite number of modes N. We multiply both sides of equation (4.5) by $\cos l\kappa x$, integrate over $\kappa x = [0{:}2\pi]$, and invoke orthogonality:

$$2\pi A_0 \delta_{l,0} + 2\sum_{n=1}^{N} A_n \int_0^{2\pi} e^{-i|n|k\mu h(x)} \cos(n\kappa x)\cos(l\kappa x) d(\kappa x) = u_0 \int_0^{2\pi} \cos(l\kappa x) h(x) d(\kappa x). \tag{4.9}$$

Equation (4.9) is readily solved for A_n by evaluating the Fourier integrals numerically. Appendix A of Balmforth, Ierley and Young [1] gives slight modifications to this method that are useful when the topography is near critical.

To account for the effect of weak viscosity on the propagating beams, then $\psi(x, z) = \sum_{n=-\infty}^{\infty} \psi_n(z) e^{in\kappa x}$ must satisfy the viscous version of equation (3.37) away from the topography. Substituting ψ into equation (3.37) gives

$$\omega^2 \left[\psi_n'' - (n\kappa)^2 \psi_n\right] + N^2 (n\kappa)^2 \psi_n - i\omega\nu \left[(n\kappa)^4 \psi_n - 2(n\kappa)^2 \psi_n'' + \psi_n''''\right] = 0. \tag{4.10}$$

Equation (4.10) has a linear solution $\psi_n(z) = A_n e^{m_n z}$, where the roots m_n must satisfy the characteristic polynomial

$$m_n^4 - \left[2(n\kappa)^2 + \frac{i\omega}{\nu}\right] m_n^2 + (n\kappa)^4 + \frac{i\omega}{\nu}(n\kappa)^2 \frac{N^2 - \omega^2}{\omega^2} = 0. \tag{4.11}$$

The four roots are found numerically, but we only retain one of the corresponding linear terms. Two of these terms are discarded because the corresponding roots of equation (4.11) have positive real parts and therefore do not satisfy the radiation condition, since the amplitude of the disturbance would grow for increasing z, which is the direction of wave propagation for subcritical topographies. Of the remaining two terms, one corresponds to the solution that satisfies the viscous, no-slip boundary condition inside the thin Stokes' layer. This decays very quickly because the root has a large real part of $O(\sqrt{\nu/\omega})$, so the solution is small compared to the inviscid solution in the far field and it can be neglected. Neglecting this solution far out weights the inconvenience of solving numerically for its modal amplitudes. Instead of solving equation (4.9) alone, this would require solving simultaneous matrix equations in which some of the matrices would become singular for near critical values of ε.

The remaining term is approximately equivalent to a weakly viscous correction to the inviscid solution. The inviscid problem is recovered by multiplying equation (4.11) by ν and setting $\nu = 0$, giving the inviscid roots

$$m_{n,inv}^2 = -(n\kappa)^2 \frac{N^2 - \omega^2}{\omega^2}. \tag{4.12}$$

If $\nu \ll 1$, as in the experiment, the inviscid root corrected to the leading order in ν is

$$m_n^2 \approx m_{n,inv}^2 + \nu m_{n,vis}^2, \tag{4.13}$$

where $m_{n,vis}$ can be found by substituting expressions (4.12) and (4.13) into equation (4.11) and neglecting all higher orders of ν. The result is

$$m_{n,vis}^2 = -\frac{i}{\omega}\left(\frac{n\kappa N}{\omega}\right)^4. \tag{4.14}$$

The final solution taken to represent the perturbation streamfunction is therefore

$$\Psi(x,z,t) = \mathrm{Re}\left[\sum_{n=-\infty}^{\infty} A_n e^{m_n z} e^{in\kappa x} e^{-i\omega t}\right], \tag{4.15}$$

where A_n are the coefficients that solve the inviscid boundary value problem, and the roots m_n allow the solution to satisfy the viscous equations in the far field approximately. For small criticality parameter ε corresponding to weak subcritical topographies, this solution approaches the solution found for a weak topography by Bell [2].

For comparison with experiments, we express the analytical wave field in terms of the perturbations to the buoyancy frequency ΔN^2. These are equivalent to the perturbations to the density gradient b_z, which can be obtained by differentiating the density distribution given by equation (3.26):

$$N^2 + \Delta N^2(x,z,t) = -\frac{g}{\rho_*}\frac{\partial \rho(x,z,t)}{\partial z} = \frac{\partial(N^2 z + b(x,z,t))}{\partial z} \tag{4.16}$$

The governing density equation (3.34) is used to find b_z given the solution obtained for the streamfunction in equation (4.15):

$$b_t = -N^2 w = -N^2\,\mathrm{Re}[\psi_x(x,z)e^{-i\omega t}]. \tag{4.17}$$

Since the solution is time harmonic, so is the perturbation to the buoyancy $b = \mathrm{Re}[b_0 e^{-i\omega t}]$, therefore

$$(b_t)_z = \omega\frac{\partial\left(-\mathrm{Re}[b_0]\sin(\omega t) + \mathrm{Im}[b_0]\cos(\omega t)\right)}{\partial z} = -N^2(\mathrm{Re}[\psi_{x,z}]\cos(\omega t) + \mathrm{Im}[\psi_{x,z}]\sin(\omega t)). \tag{4.18}$$

The components $\mathrm{Re}[b_0]$ and $\mathrm{Im}[b_0]$ are found by comparing the coefficients of the sines and cosines in the equation above, to re-construct

$$\Delta N^2 = b_z = \frac{N^2}{\omega}\left[\mathrm{Im}[\psi_{x,z}]\cos(\omega t) - \mathrm{Re}[\psi_{x,z}]\sin(\omega t)\right]. \tag{4.19}$$

4.2 Experimental results

Two experiments were performed by oscillating a Gaussian ridge back and forth in the experimental stratification; and the resulting wave fields were compared to Balmforth, Ierley and Young's [1] linear theory. The topography was $h_0 = 14.7 \pm 0.2\,\text{mm}$-tall and had a standard deviation of $\sigma = 20\,\text{mm}$. It's characteristic horizontal scale was $k^{-1} = 4\sigma = 80\,\text{mm}$ and it's maximum slope was $h'_{\text{max}} = -(h_0/\sigma)\exp(-1/2) = 0.45$, which corresponds to a 24° inclination from the horizontal. The forcing frequency was changed to generate steep, subcritical wave beams in one experiment and shallow beams at almost the critical slope in the second experiment; and the excursion was short in both to ensure linear wave fields. The parameters for the two experiments are summarized in table 4.2.1 below.

Table 4.2.1 Gaussian experiments parameters

Gaussian	ω(rad/s)	N(rad/s)	θ(°)	ε	u_0(mm/s)	ku_0/ω
Experiment 1	1.020	1.23	55.8	0.30	2.88	0.035
Experiment 2	0.527	1.23	25.1	0.94	1.59	0.038

These experiments were planned to test the linear model throughout the range of non-dimensional parameters for which it is valid: namely, where the criticality parameter is arbitrarily below criticality $\varepsilon < 1$ and the excursion parameter is small $ku_0/\omega \ll 1$. The second experiment was particularly interesting because it was at the limit of criticality, and also because shallow beams are more common in the ocean, where typically $\alpha = \tan\theta \approx 0.1$. Furthermore, the forcing was in the frequency range $2\omega < N$, such that if second harmonic wave beams were to be generated, they would be able to propagate at $\theta = \sin^{-1}(2\omega/N)$, as discussed in section 1.2. Second harmonic wave beams would be generated by nonlinear interactions in the local wave field, which has been observed in numerical simulations of super critical generation by Lamb [17]; and also by a lee-wave mechanism as the excursion parameter is increased, as in Bell's lee-wave theory for weak topography [2].

4.2.1 Subcritical wave beams

For the first experiment the topography was oscillated at $\omega = 1.020 \pm 0.001\,\text{rad/s}$ in a stratification of $N = 1.23 \pm 0.02\,\text{rad/s}$, so the beams propagated at $\theta = 55.8 \pm 0.5^\circ$ to the hor-

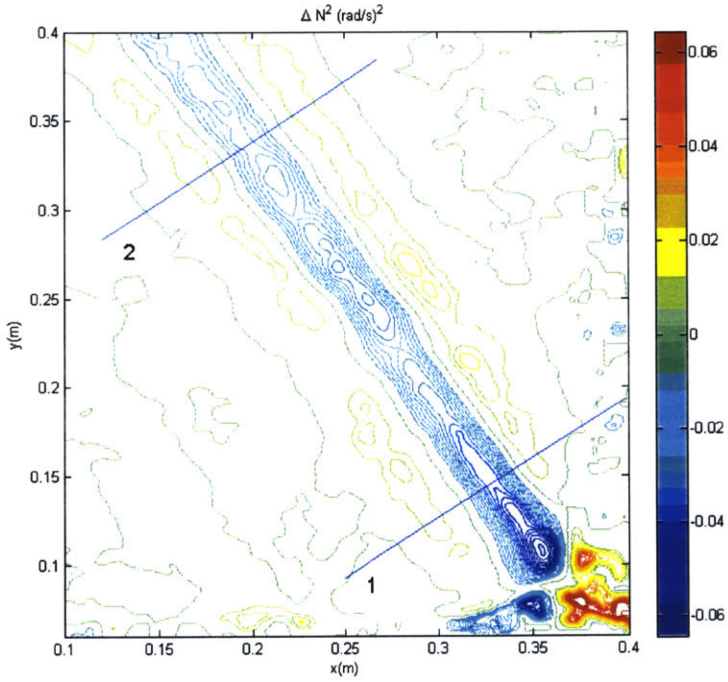

Figure 4-2: Contours of ΔN^2 for the experimental wave field generated over a Gaussian ridge. The wave beam propagates at 55.8 ° from the horizontal.

izontal. The criticality parameter was $\varepsilon = 0.30 \pm 0.1$. The maximum forcing velocity was $u_0 = 2.88 \pm 0.03\,\mathrm{mm/\,s}$, therefore the excursion parameter was small $ku_0/\omega = 0.035 \pm 0.004$. A movie was captured showing the apparent distortion of pattern of dots behind the tank during the oscillation of the topography.

A wave beam is seen clearly in figure 4-2, which shows the contours of the perturbations to the density gradient $\triangle N^2$ in a snapshot of the wave field generated by the oscillating ridge. The location of the ridge would correspond to the bottom right-hand side of figure 4-2. This image was obtained from a single frame of the movie, which was processed using DigiFlow. Note that the wave field is symmetric about the topography, yet figure 4-2 is framed around one side of the topography only in order to get a broader and more detailed view of one of the propagating beams. At the instant when this frame was captured the phase of the

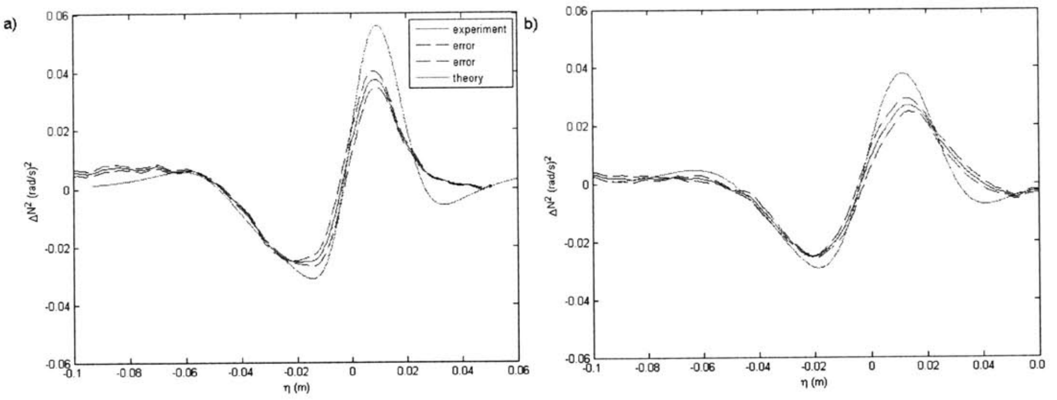

Figure 4-3: Comparisons of experimental versus theoretical values of ΔN^2 across a wave beam at $\phi = 0$. a) Comparison across cross-section 1. b) Comparison across cross-section 2.

tidal oscillation was $\phi = \omega t = 3\pi/2$. The beam propagates upward and to the left with an amplitude of $\triangle N^2 \approx 0.04(\text{rad/s})^2$ about the background stratification. The disturbance is somewhat larger over the topography, where contours indicate $\triangle N^2 \approx 0.06(\text{rad/s})^2$. There is no significant spreading or decay of the radiated wave beam, suggesting that viscosity plays a minor role in its propagation.

A direct comparison between this experiment and the wave field predicted by theory is presented in figures 4-3 and 4-4. Figure 4-3 shows comparisons of experimental versus theoretical values of ΔN^2 from left to right across the cross-sections labelled 1 and 2 in figure 4-2 at $\phi = 0$. The theoretical profiles (indicated by a soft solid line) do a good job of predicting the shape and evolution of the experimental profiles (indicated by a solid line and dashed lines at the root mean square error), but they over-predict the peak amplitude of the wave beam. Both theory and experiment show that the amplitude decays by $0.02(\text{rad/s})^2$ from location 1 to location 2; but the peaks predicted by the theory are 50% higher than the experimental ones for cross-section 1, and 40% higher for cross-section 2. Figure 4-4 shows the profiles at location 1 for instances at three additional phases of the oscillation: $\phi = \pi/2, \pi$ and $3\pi/2$. The quality of the comparison at location 1 persists throughout the entire period of the oscillation. Note also that the pairs of beam profiles with phase difference of π ($\pi/2$ versus $3\pi/2$ and π versus 2π)

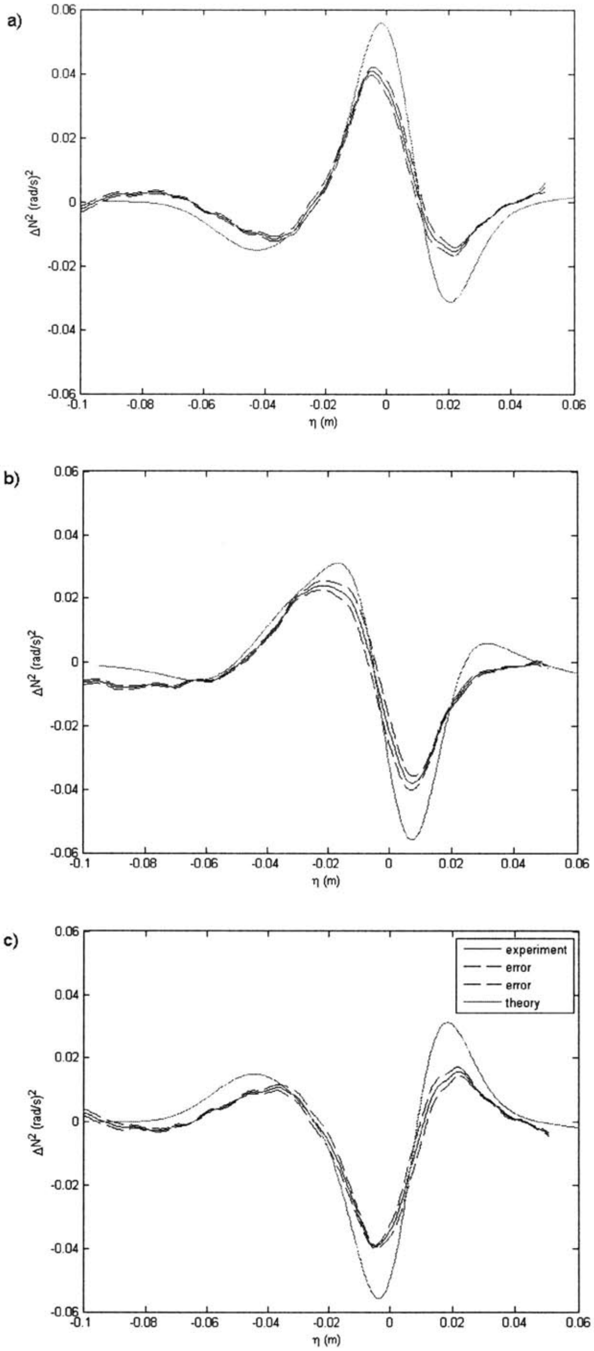

Figure 4-4: Comparisons of experimental versus theoretical values of ΔN^2 at cross-section 1 and different instances in the phase of oscillation. a) $\phi = \pi/2$, b) $\phi = \pi$, c) $\phi = 3\pi/2$.

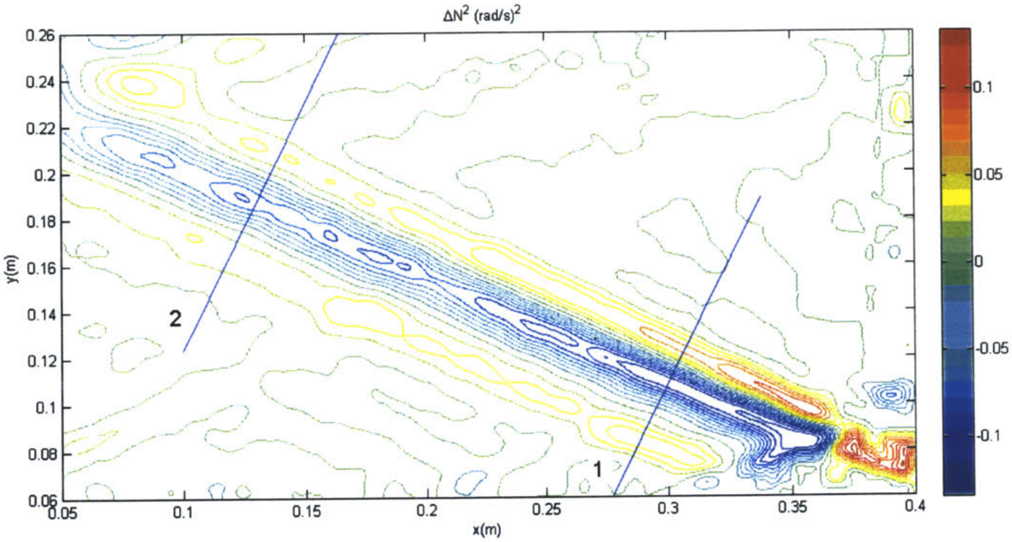

Figure 4-5: Contours of ΔN^2 for the experimental wave field generated over a Gaussian ridge. The wave beam propagates at 25.1 ° from the horizontal.

are mirror images of each other, which confirms that the forcing achieved with the apparatus is symmetric.

4.2.2 Near critical wave beams

For this experiment the topography was oscillated at $\omega = 0.527 \pm 0.001\,\mathrm{rad/s}$ in the same stratification as above, so the beams propagated at $\theta = 25.1 \pm 0.5\,°$ to the horizontal. The criticality parameter was $\varepsilon = 0.94 \pm 0.1$. The maximum forcing velocity was $u_0 = 1.59 \pm 0.03\,\mathrm{mm/s}$, and excursion parameter was $ku_0/\omega = 0.038 \pm 0.004$.

Figure 4-5 shows the contours of the perturbations to the density gradient $\triangle N^2$ in a snapshot of the wave field at $\phi = 0$. The propagating wave beam is stronger than the more subcritical one in figure 4-2, with an amplitude of $\triangle N^2 \approx 0.06(\mathrm{rad/s})^2$ about the background stratification. The disturbance over the topography is as large as $\triangle N^2 \approx 0.09(\mathrm{rad/s})^2$, but once again there is no major spreading or decay. Note also that there is no clear indication in the wave field of a second harmonic beam propagating at 58.9 ° to the horizontal, which confirms that the wave field right above the topography is linear.

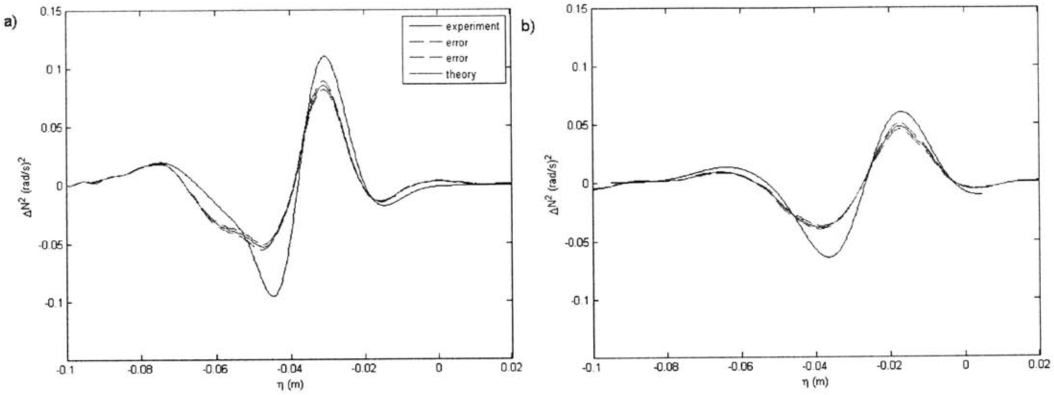

Figure 4-6: Comparisons of experimental versus theoretical values of ΔN^2 across a wave beam at $\phi = 0$. a) Comparison across cross-section 1. b) Comparison across cross-section 2.

Figure 4-6 shows comparisons of experimental versus theoretical values of ΔN^2 from across the cross-sections labelled 1 and 2 in figure 4-5. The comparison between the theoretical and experimental profiles is very similar to the comparison for the previous experiment. The theoretical profiles do a good job of predicting the shape and evolution of the experimental profiles, but they over-predict the peak amplitude of the wave beam. Both theory and experiment show that the amplitude decays by $0.04(\mathrm{rad/s})^2$ from location 1 to location 2; but the peaks predicted by the theory are 30% higher than the experimental ones for cross-section 1, and 20% higher for cross-section 2. There is also a distortion at the left-hand side of the beam profiles at cross-section 1, which corresponds to the region closest to the bottom boundary. It is reasonable to expect some disagreement between experiment and theory in this area, as the experiment may see disturbances in the wave field excited over the moving surface. Finally, figure 4-7 shows the profiles at location 1 for instances at three additional phases of the oscillation: $\phi = \pi/2$, π and $3\pi/2$.

A detailed discussion of these results is presented in the discussion in Chapter 6.

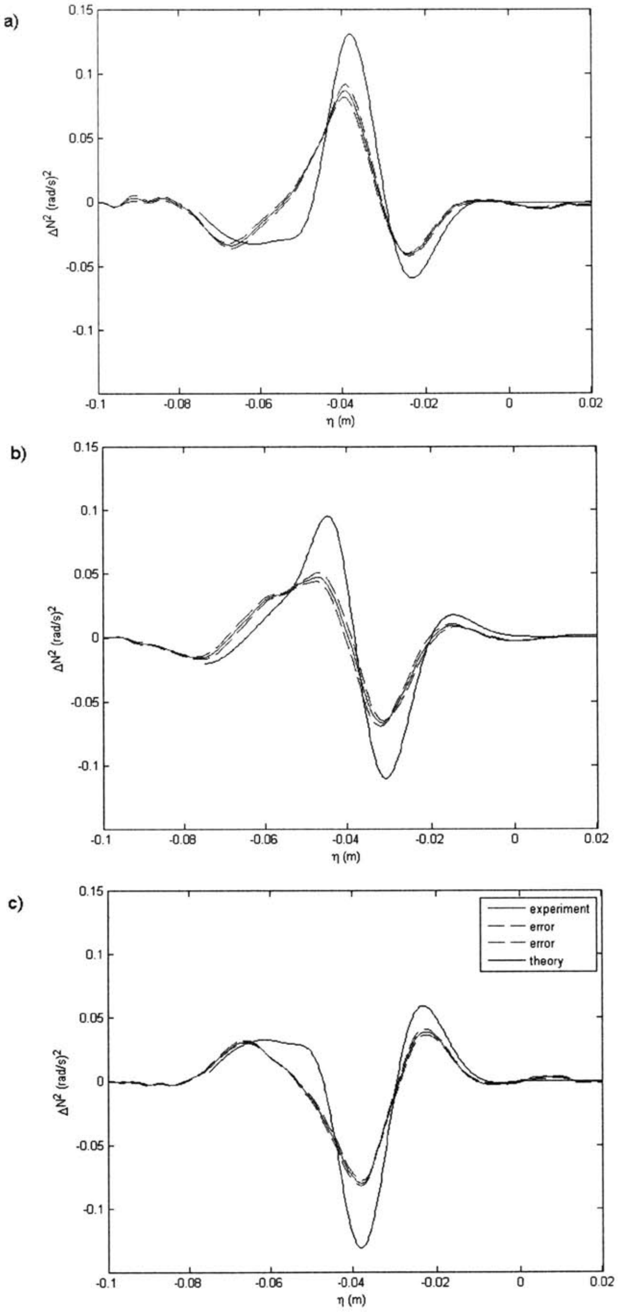

Figure 4-7: Comparisons of experimental versus theoretical values of ΔN^2 at cross-section 1 and different instances in the phase of oscillation. a) $\phi = \pi/2$, b) $\phi = \pi$, c) $\phi = 3\pi/2$.

Chapter 5

Generation at a knife-edge

The solution to the problem of internal tide generation by a knife-edge can be extracted from the solution for an oscillating ellipse by Hurley and Keady [15] or from the solution for tidal flow over a triangular ridge by Llewellyn Smith and Young [22]. In this chapter, Hurley and Keady's solution is reviewed and compared with experimental results. This formulation was chosen because it is geared toward the calculation of the analytical wave field, as is the experimental method, whereas Llewellyn Smith and Young's solution is concerned with the calculation of the total energy flux. Indeed, Smith and Young show in their paper that their solution for a knife-edge is a special case of Hurley and Keady's solution [22].

Two experiments were performed seeking to achieve a linear regime, and the results show good agreement with the theoretical solution and an absence of nonlinear effects.

5.1 Analytical solution

The generation of internal waves by an oscillating elliptical cylinder can be studied with respect to a set of coordinates (s, σ) that are aligned tangential and perpendicular to the wave beams, namely

$$s = x\cos\theta + z\sin\theta \ \text{ and } \sigma = x\sin\theta - z\cos\theta, \tag{5.1}$$

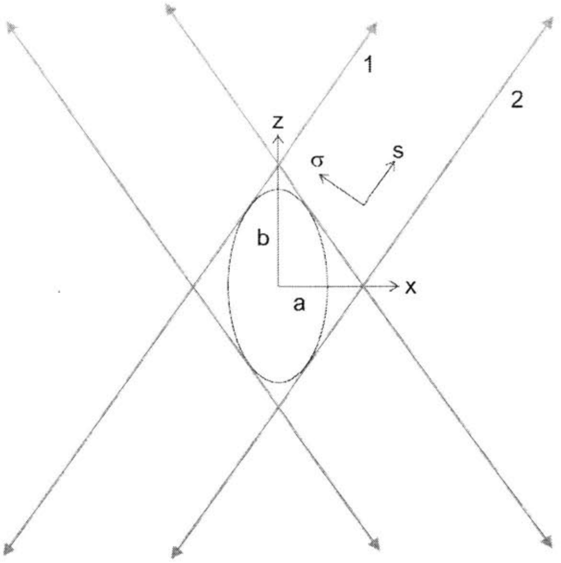

Figure 5-1: Oscillating ellipse configuration and definition of coordinates (s, σ). We consider the wave beams labelled 1 and 2 that propagate upwards and to the right.

for waves propagating from the topography at an angle θ in the upper-right quadrant. This is shown in figure (5-1). Equation (3.37) can be written in terms of (s, σ) as

$$\frac{\partial^2 \psi}{\partial \sigma \partial s} + \cot(2\theta) \frac{\partial^2 \psi}{\partial s^2} + i\lambda a'^2 \nabla^4 \psi = 0, \tag{5.2}$$

where $\lambda = \nu\alpha / 2\omega a'^2 = \alpha(\delta/a')^2/2$, δ is the thickness of the Stokes' layer and a' is a characteristic dimension of the cylinder in the (x, z) plane. For the inviscid problem, the last term in equation (5.2) is zero, and the boundary condition on the topography is

$$\psi\left(\frac{x^2}{a^2} + \frac{z^2}{b^2} = 1\right) = -U_0 z, \tag{5.3}$$

where a and b denote the horizontal and vertical semi-axes of the elliptical cylinder.

Hurley and Keady first seek a solution to inviscid generation by an elliptical cylinder [14]. The problem is mapped onto a new complex plane through a Joukowski transformation, by which the elliptical cylinder in $z_0 = x + iz$ becomes a circular cylinder of radius $a_1 = (a + b)/2$

in z_1, where

$$z_1 = z_0 + \frac{a^2 - b^2}{4z_0}. \tag{5.4}$$

By imposing this transformation onto equations (5.2) and (5.3), the following solution is found to satisfy the inviscid boundary condition:

$$\psi_{inv}(s,\sigma) = -i\beta c \int_0^\infty \frac{J_1(\kappa)}{\kappa} e^{i\kappa\sigma/c} d\kappa, \tag{5.5}$$

where $c^2 = a^2 \sin^2\theta + b^2 \cos^2\theta$ and $\beta = \left(b^2 u_0 \cos\theta - iabu_0 \sin\theta\right)/2c^2$.

A corrected solution is proposed to satisfy the viscous governing equations along the propagating beam:

$$\psi(s,\sigma) = -i\beta c \int_0^\infty \frac{J_1(\kappa)}{\kappa} e^{ms/c} e^{i\kappa\sigma/c} d\kappa, \tag{5.6}$$

where the roots m must satisfy the polynomial

$$m^4 - m^2\left(2\kappa^2 + i\frac{\cot(2\theta)}{\lambda}\right) + m\frac{\kappa}{\lambda} + \kappa^4 = 0. \tag{5.7}$$

The two roots m that satisfy the radiation condition, by which the wave must decay along s, have a negative real part. The fast-decaying root corresponds to the Stokes' layer that can be neglected in the far field. The slow-decaying root can be approximated taking a boundary layer approach [37]: assuming that the wave beam propagates uniformly along s, such that $\partial/\partial s \ll \partial/\partial\sigma$, one can neglect the derivatives along the beam with respect to the derivatives across the beam, so equation (5.2) is approximately

$$\frac{\partial^2\psi}{\partial\sigma\partial s} + i\lambda a'^2 \frac{\partial^4\psi}{\partial\sigma^4} = 0. \tag{5.8}$$

The general solution in equation (5.6) satisfies equation (5.8) when $m = m_{approx} = -\lambda\kappa^3$. Hurley and Keady show that for a weakly viscous flow where $\lambda \ll 1$, the slow-decaying root of equation (5.7) approaches this approximate value, and therefore take $m = m_{approx}$ in their solution. Note also that approaching the topography from the far field, as $s \to c$, the viscous solution ψ approaches the inviscid solution ψ_{inv} continuously as the integral of $e^{\lambda s/c}$. Since ψ_{inv} exactly satisfies the inviscid boundary condition in (5.3); thus, for $\lambda \ll 1$, ψ approximately

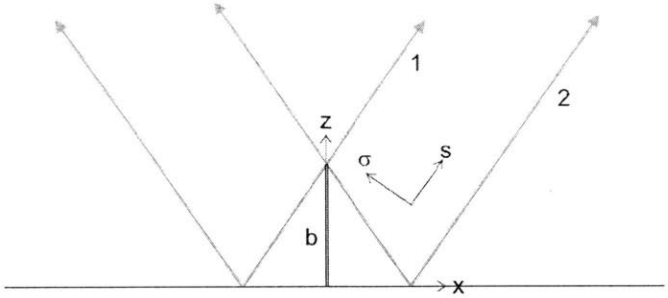

Figure 5-2: Knife edge configuration. The wave beams that propagate upwards and to the right are again labelled 1 (radiated off the top of the topography) and 2 (reflected off the bottom surface).

satisfies equation (5.3).

With one semi-axis of the ellipse and the tidal forcing horizontal, the streamfunction associated with the wave beam radiated in the upper-right quadrant is described by

$$\psi_+(x,z) = -i\beta c \int_0^\infty \frac{J_1(k)}{k} \exp\left(-\frac{k^3\nu\alpha}{2c^2\omega}\frac{x\cos\theta + z\sin\theta}{c} + ik\frac{x\sin\theta - z\cos\theta}{c}\right) dk. \tag{5.9}$$

For the knife-edge topography $a = 0$ and $b = h_0$, in which case equation (5.9) simplifies to

$$\psi(x,z) = -\frac{i}{2}u_0 h_0 \int_0^\infty \frac{J_1(k)}{k} \exp\left[-\left(\frac{k\alpha}{h_0}\right)^3 \frac{\nu(x+\alpha z)(1+1/\alpha^2)}{2\omega} + i\frac{k\alpha}{h_0}(x - z/\alpha)\right] dk. \tag{5.10}$$

Note that the solution given by equation (5.10) is also valid for the downward propagating beam that reflects off the bottom surface as shown in figure (5-2). This is equivalent to the wave beam that radiates from the bottom of the ellipse directly onto the first quadrant, which is labelled as beam 2 in figure 5-1.

To find ΔN^2, the integrand of equation (5.10) is multiplied by the pre-factor

$$\left(\frac{k\alpha}{h_0}\right)^2 \left[-\nu\left(\frac{k\alpha}{h_0}\right)^2 \frac{1+1/\alpha^2}{2\omega} + i\right] \left[-\nu\alpha\left(\frac{k\alpha}{h_0}\right)^2 \frac{1+1/\alpha^2}{2\omega} - i/\alpha\right], \tag{5.11}$$

corresponding to the derivatives of the streamline with respect to x and z, and the resulting integral can be solved numerically. Then ΔN^2 is reconstructed as specified in equation (4.19).

An important short-coming of this model is that the linear problem assumes $ku_0/\omega = A/k^{-1} \ll 1$, whereas for any thin knife-edge the horizontal spatial scale $k^{-1} = a \to 0$, so ku_0/ω will be large even for small forcing amplitudes A. Therefore, the nonlinear terms that are neglected in equations (3.7) to (3.9) may have a significant effect on the wave field that is not predicted by theory. The experiments presented in the following section aimed to investigate the validity of this model for different excursion amplitudes.

5.2 Experiment results

Two experiments were performed using a knife-edge topography and the resulting wave fields were compared to Hurley and Keady's [15] linear theory. The topography used was $h_0 = 16.0 \pm 0.2$ mm-tall and 1.0 ± 0.2 mm-wide. The forcing frequency was changed to vary the angle of propagation of the wave beams and the forcing excursion was maintained as low as possible in an attempt to achieve linear generation. The parameters for the two experiments are summarized in table 5.2.1 below.

Table 5.2.1: Knife edge experiments parameters

Knife edge	ω(rad/s)	N(rad/s)	θ(°)	u_0(mm/s)	ku_0/ω
Experiment 1	1.020	1.19	57.6	0.84	0.82
Experiment 2	0.527	1.19	25.3	0.59	1.03

5.2.1 Steep wave beams

For the first experiment the topography was oscillated at $\omega = 1.020 \pm 0.001$ rad/s in a stratification of $N = 1.19 \pm 0.02$ rad/s, so the beams propagated at $\theta = 57.6 \pm 0.5°$ to the horizontal. The maximum forcing velocity was $u_0 = 0.84 \pm 0.03$ mm/s and the excursion parameter was large $ku_0/\omega = 0.82 \pm 0.03$.

Figure 5-3 shows the contours of the perturbations to the density gradient $\triangle N^2$ in a snapshot of the wave field generated by the oscillating knife-edge, which was located at the bottom left-hand side of the frame. At the instant of this frame the phase of the oscillation was $\phi = 0$. Since the topography was supercritical, two wave beams were radiated off the top of the knife-edge: one beam propagated upward and the second beam propagated downward and reflected off the

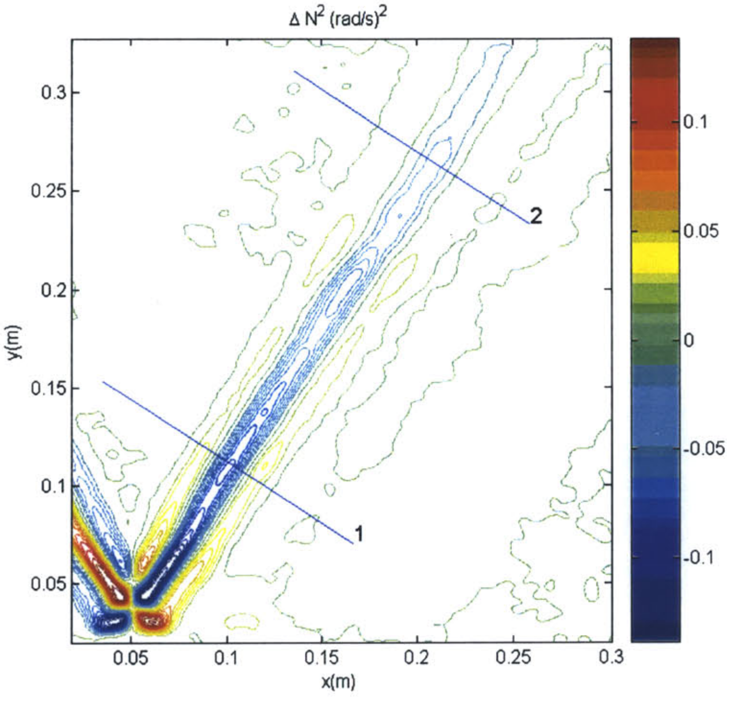

Figure 5-3: Contours of ΔN^2 for the experimental wave field generated over a knife-edge. The wave beam propagates at 57.6 ° from the horizontal.

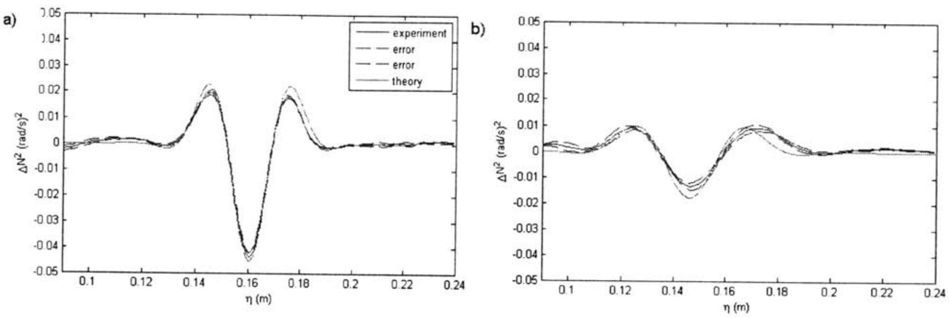

Figure 5-4: Comparisons of experimental versus theoretical values of ΔN^2 across a wave beam at $\phi = 0$. a) Comparison across cross-section 1. b) Comparison across cross-section 2.

bottom surface. The combined wave beam is seen in the far field in figure 5-3 propagating upward with an amplitude around $\triangle N^2 \approx 0.03(\mathrm{rad/s})^2$ about the background stratification.

Another interesting feature of the wave field is that local disturbances over the knife-edge were very large, reaching $\triangle N^2 > 0.10(\mathrm{rad/s})^2$. Beyond this region the signal strength decayed quickly and the width of the wave beam spread out. In fact, the distortions of the image close to the knife-edge were so strong that synthetic Schlieren was no longer valid, so the contour plot does not provide detailed information in this region. Such strong local disturbances were not observed over the Gaussian ridge, and indeed it would be expected to find stronger disturbances over the knife-edge, which is a more dramatic feature and both the criticality and the excursion parameters are larger in these experiments. The wave beam in figure 5-3 also appears to spread more and decay faster than the beams in the subcritical experiments, suggesting that viscosity plays a more important role in the evolution of the wave field generated at a knife-edge.

A direct comparison between this experiment and the wave field predicted by theory is presented in figures 5-4 and 5-5. Figure 5-4 shows comparisons of experimental versus theoretical values of ΔN^2 from right to left across the cross-sections labelled 1 and 2 in figure 5-3. The theoretical profiles (indicated by a solid line) closely predict the amplitude, shape, and evolution of the experimental profiles (indicated by a soft solid line and dashed lines at the root mean square error). Both theory and experiment show that the amplitude of the wave beam decays by almost 50% from location 1 to location 2; and that the width of the beam spreads from 6 cm-wide at location 1 to almost 10 cm-wide at location 2. The deviations in

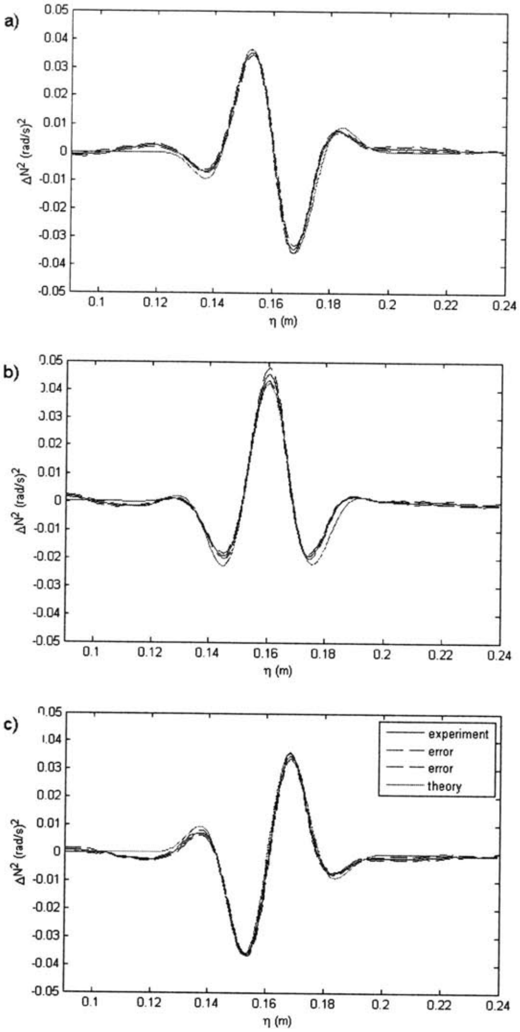

Figure 5-5: Comparisons of experimental versus theoretical values of ΔN^2 at cross-section 1 and different instances in the phase of oscillation. a) $\phi = \pi/2$, b) $\phi = \pi$, c) $\phi = 3\pi/2$.

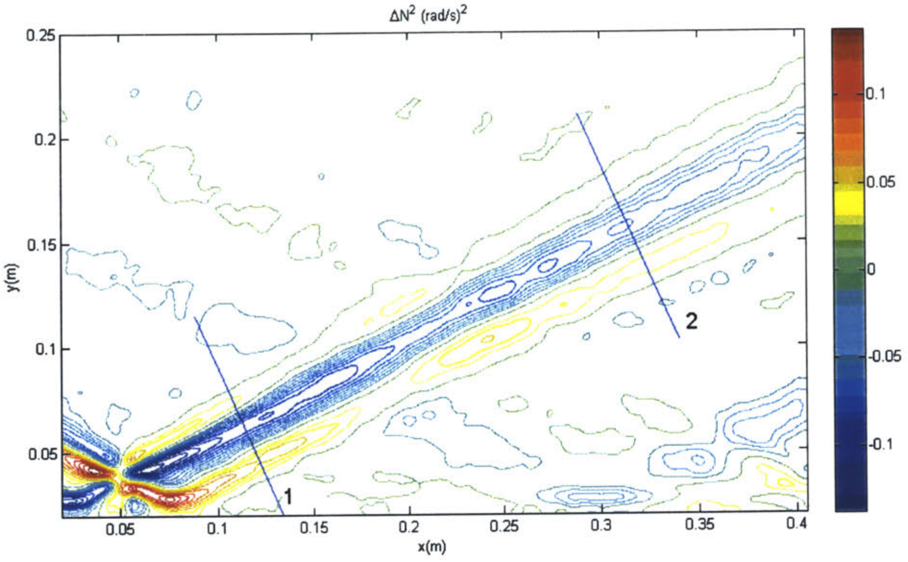

Figure 5-6: Contours of ΔN^2 for the experimental wave field generated over a knife-edge. The wave beam propagates at 25.3 ° from the horizontal.

the wave amplitude between the theoretical and experimental profiles are less than 10% for cross-section 1 and less than 20% for cross-section 2, at which point the experimental profile is not as accurate because the signal is weak. Figure 5-5 shows the profiles at location 1 for instances at three additional phases of the oscillation: $\phi = \pi/2$, π and $3\pi/2$. The quality of the comparison at location 1 persists throughout the entire period of the oscillation.

5.2.2 Shallow wave beams

The second experiment was performed to investigate shallow wave beams. The topography was oscillated at $\omega = 0.527 \pm 0.001\,\mathrm{rad/s}$ in the same stratification, so the beams propagated at $\theta = 25.3 \pm 0.5\,^\circ$ to the horizontal. The maximum forcing velocity was $u_0 = 0.59 \pm 0.03\,\mathrm{mm/s}$, which is representative of the slowest motion obtained reliably from the apparatus, but still accounts for a large excursion parameter $ku_0/\omega = 1.03 \pm 0.03$.

Figure 5-6 shows the contours of $\triangle N^2$ in a snapshot of the experiment when the phase of the oscillation was $\phi = 0$. The two wave beams radiated off the top of the knife-edge

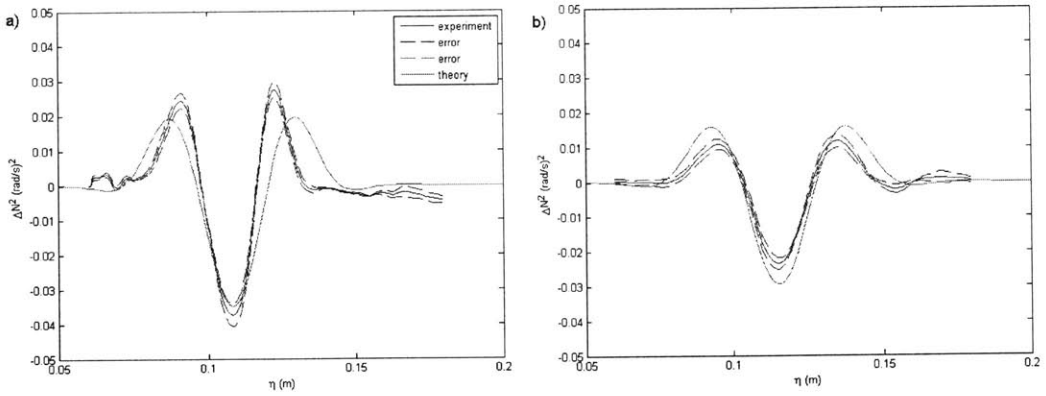

Figure 5-7: Comparisons of experimental versus theoretical values of ΔN^2 across a wave beam at $\phi = 0$. a) Comparison across cross-section 1. b) Comparison across cross-section 2.

and the reflection of the downward propagating beam are easier to distinguish in this image because of the geometry. The local disturbances observed over the knife-edge were still strong, with amplitudes up to $\triangle N^2 \approx 0.06(\mathrm{rad/s})^2$, yet not as strong as in the previous experiment described, possibly because in this shallow beam experiment the amplitude of the tidal forcing was slightly lower. The wave beam in figure 5-6 also appears to spread out and decay, although the decay is not as dramatic as for the wave beam in figure 5-6, so the amplitude of the wave beam in the far field is still around $\triangle N^2 \approx 0.03(\mathrm{rad/s})^2$ about the background stratification. There are also weak disturbances to the background in the upper left-hand side and the lower right-hand side of the frame, caused by a weak reflection of the wave beam off the damping material on the right wall of the tank.

Most notably, there is no evidence of second harmonic beams propagating at 62.5 ° to the horizontal. This indicates that, despite generation being highly supercritical and the excursion being long, the radiated wave field was still essentially linear.

Figures 5-7 and 5-8 show the comparisons of experimental versus theoretical values of ΔN^2 across the cross-sections of the wave beam labelled 1 and 2 in figure 5-6; and for $\phi = \pi/2$, π and $3\pi/2$ at cross-section 1. The comparisons along the beam and throughout one oscillation are still good, although some discrepancies arise that are not present in the steep wave beam

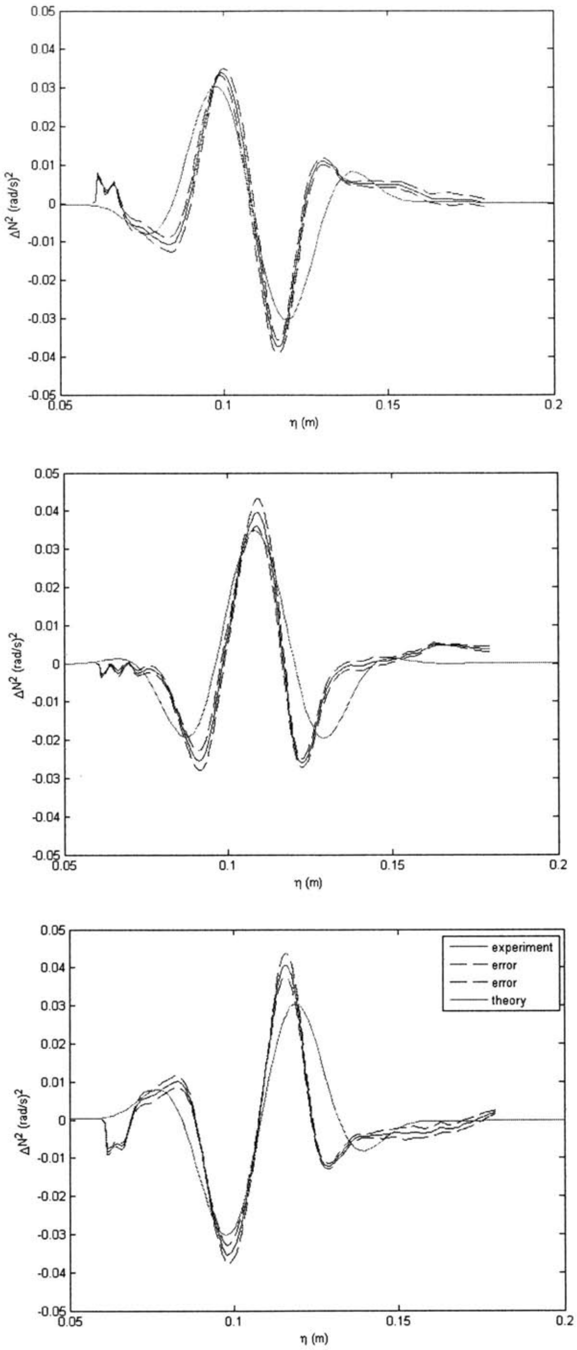

Figure 5-8: Comparisons of experimental versus theoretical values of ΔN^2 at cross-section 1 and different instances in the phase of oscillation. a) $\phi = \pi/2$, b) $\phi = \pi$, c) $\phi = 3\pi/2$.

experiment. The theoretical wave beam decays about 15% in amplitude and spreads from 16.5 to 18 cm from location 1 to location 2. The experimental wave beam decays almost 30% in amplitude and spreads in width from 9 to 12 cm. Thus, the experimental wave beam is narrower and decays faster than the theoretical prediction.

It is worth noting, however, that the two extremes of the experimental profiles at cross-section 1 are affected by disturbances in the flow field that are unaccounted for by the theory: below the beam, the edge between the topography and the moving surface, although smooth, causes a disturbance (on the left side of the profiles in figures 5-7 and 5-8); and above the beam the cross-section cuts near the weak reflection from the side wall (on the right side of the profiles). These disturbances affect the amplitude of the profile at either side of the wave beam cross-section, as can be seen in the profiles in figure 5-8: they cause the small bumps at the left and the distortion of the profile at the right. In changing the shape of the profile slightly these disturbances also change the effective width of the beam. Overall they contribute to the discrepancies in the comparison of the experimental versus the theoretical profiles.

Chapter 6

Discussion of results

Chapters 4 and 5 present the comparisons between quantitative experimental wave fields and theoretical wave fields for internal tide generation by 2D topography. Care was taken to perform experiments in the linear regimes where the theory is formally valid, and the comparisons are indeed in good agreement. In particular we see that the theory does a good job of describing the shape and evolution of the wave beams; Balmforth, Ierley and Young's theory [1] for the Gaussian topography does a reasonable job of predicting the wave field amplitude, and Hurley and Keady's [15] theory applied to generation by a knife-edge is accurate in describing the amplitude of the internal wave beam, to within experimental errors.

6.1 Linear wave fields

A good indication of the linearity of the wave fields investigated is the absence of a clear second harmonic signal in the shallow wave beam experiment performed with the knife-edge topography. Figure 6-1 shows contours of ΔN^2 for a full frame view of the wave field around the knife-edge (for a different experimental run with the same forcing amplitude $A = 0.64 \pm 0.05$ mm and angle of beam propagation). The knife-edge experiments resulted in the most nonlinear wave fields among the experiments described above, because generation was highly supercritical and the excursion parameter was not small. The fact that these nonlinearities were not strong enough to generate second harmonic beams confirms that, in order to describe this wave field, it was valid to neglect the advective terms and linearize the governing equations in chapter 3.

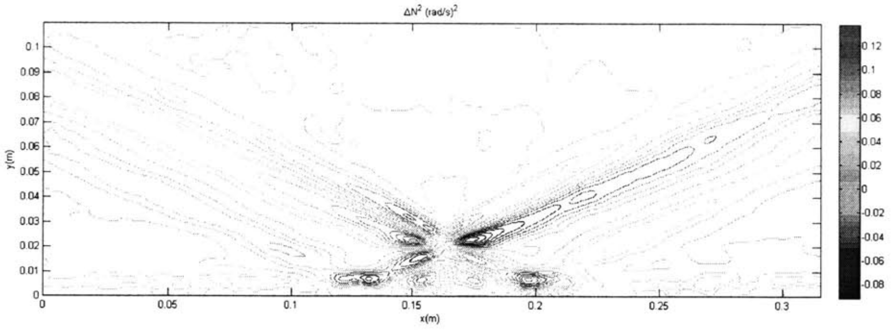

Figure 6-1: Full-frame contour plot of ΔN^2 in the wave field around a 25 ° beam. The forcing was $A = 0.65 \pm 0.05$ mm.

The perturbations in figure 6-1 go down to $\Delta N^2 \approx -0.05(\mathrm{rad/s})^2$ about a background $N^2 = O(1)$. Clearly, the perturbations would not be strong enough to reverse the stable stratification.

6.2 The role of viscosity on wave beam stability

The experiment results show that viscosity plays an interesting role in the structure of the radiated wave beams. The experimental wave fields over the knife-edge (in figures 5-3 and 5-6) showed significant decay and spreading away from the topography, suggesting a large viscosity effect; whereas the experimental wave fields achieved with the Gaussian ridge (figures 4-2 and 4-5) showed minor decay of the propagating beam. A good indication of the effect of viscosity in the wave beams can be obtained by comparing theoretical profiles of $\triangle N^2$ across the beams radiated off each topographic feature for different values of viscosity. This is shown in figure 6-2, where the profiles shown are taken at the cross-sections labelled 1 in figures 5-3 and 4-2, respectively. By decreasing the value of the viscosity coefficient ν by an order of magnitude (from $1.1 \times 10^{-6}\,\mathrm{m^2/s}$ to $1 \times 10^{-7}\,\mathrm{m^2/s}$) the wave beam radiated off the knife-edge changed dramatically and became a very sharp disturbance: it's amplitude increased by 250% and it's width decreased by almost a factor of 2. This change in viscosity corresponds to an increase in Reynolds number from Re = 3 to 34. On the other hand, for the same change in viscosity,

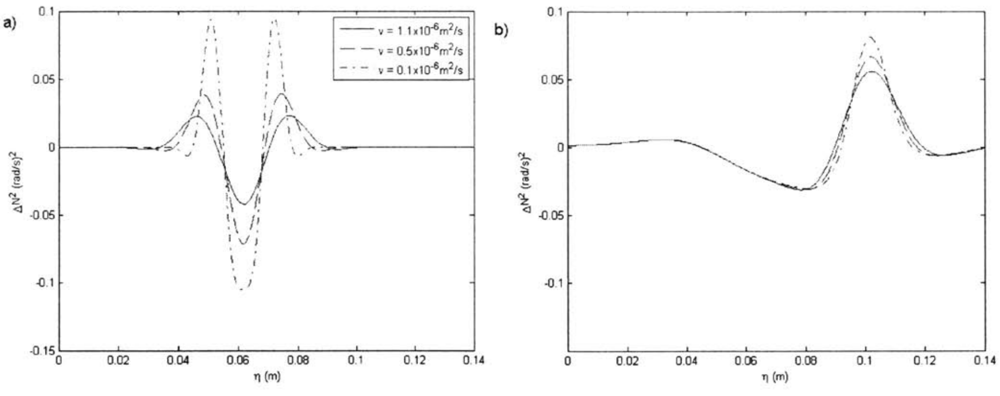

Figure 6-2: Profiles of ΔN^2 for decreasing values of viscosity. Both profiles are taken at cross sections 1 for a) the knife-edge experiment in figure 5-3, and b) the Gaussian ridge experiment in figure 4-2.

the wave field radiated off the Gaussian ridge only changed slightly: it's amplitude increased by 40% and it's width was not changed noticeably. The increase in Reynolds number was of the same order of magnitude, from Re = 209 to 2300.

Viscosity smoothed out strong features in the supercritical wave field such that the wave beams remained stable to buoyancy and shear, contrary to the predictions of inviscid linear theory. Balmforth, Ierley and Young [1] observe that, for generation problems with large subcritical ε and strong forcing, the inviscid linear model used in this paper predicts buoyancy instabilities (reversals in the vertical stratification) along radiated wave beams. Petrelis et. al. [30] note the same in their inviscid and hydrostatic solution to supercritical generation. These reversals of the stratification can be seen in figure 6-3 from Balmforth, Ierley and Young [1], which shows the contours of constant buoyancy $N^2 z + b$ for generation by a Gaussian topography with long excursion and criticality increasing from $\varepsilon = 0.2$ to 0.8. A buoyancy instability criteria is the condition

$$\frac{\partial(N^2 z + b)}{\partial z} = N^2 + \triangle N^2 < 0, \tag{6.1}$$

which is satisfied for $\varepsilon > 0.5$ and large excursion in figure 6-3. On the other hand the wave

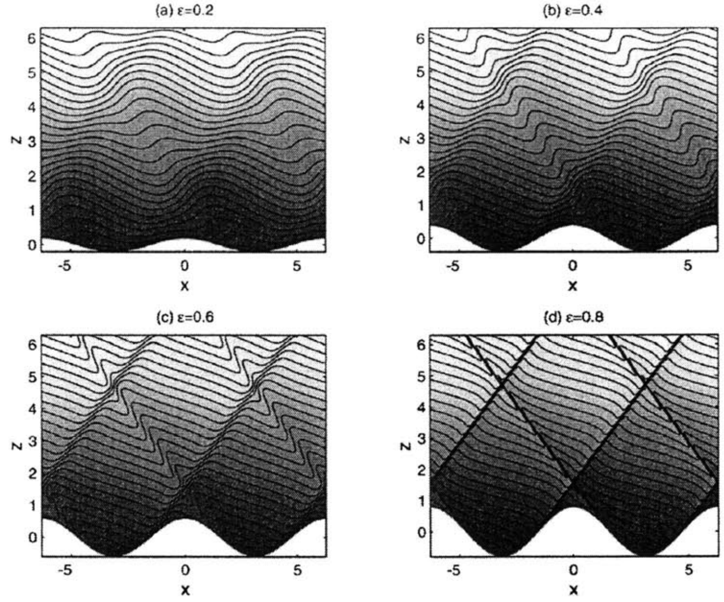

Figure 6-3: Snapshots of the buoyancy field for large excursions such that $\varepsilon u_0 k/\omega = 1/2$ and criticality parameters are a) $\varepsilon = 0.2$, b) $\varepsilon = 0.4$, c) $\varepsilon = 0.6$, and d) $\varepsilon = 0.8$. From Balmforth, Ierley and Young.

beams observed in the experiments presented here were all stable to buoyancy, since the negative perturbations to the stratification along the wave beam were at most $\triangle N^2 = -0.05(\mathrm{rad/s})^2$ over a background stratification $N^2 = 1.19(\mathrm{rad/s})^2$.

The comparisons in figure 6-2 suggest a strong dependence of instabilities on viscosity at the low Reynolds numbers found in the laboratory. A generation scenario with higher Reynolds number but the same excursion and high criticality parameters could result in buoyancy instabilities. This is the case for the nearly critical generation problem at the Gaussian ridge that is presented in section 4.2.2, which has $\varepsilon = 0.94$ and $ku_0/\omega = 0.038$. Figure 6-4a shows an analytical cross-beam profile of ΔN^2 that corresponds to the location of cross section 1 in figure 4-5 at $\phi = \pi$, but this time the profile was calculated for a value of viscosity $\nu = 10^{-9}\,\mathrm{m^2/s}$, which corresponds to $\mathrm{Re} = 1.3 \times 10^5$. The strong negative perturbations of the buoyancy field $\Delta N^2 = -3.9(\mathrm{rad/s})^2$ about the background stratification $N^2 = 1.51(\mathrm{rad/s})^2$ result in a buoyancy instability.

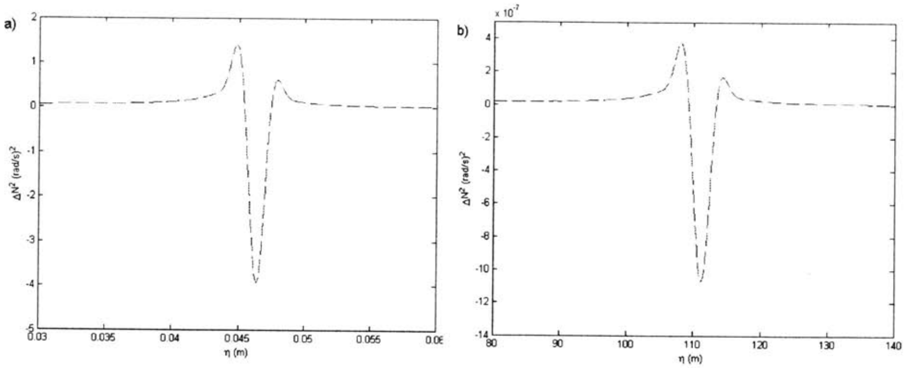

Figure 6-4: Profiles of ΔN^2 on unstable wave beams generated by a near-critical Gaussian topography at high Reynolds numbers $\mathrm{Re} = O(10^5)$. a) Analytical profile at cross section 1 for the experiment in figure 4-5 when $\nu = 10^{-9}\,\mathrm{m}^2/\mathrm{s}$. b) Analytical profile at a similar cross section for an internal tide generated over a Gaussian ridge with typical oceanic dimensions and forcing parameters.

An equivalent scenario can be conceived in the ocean. To obtain similar Reynolds number and criticality parameter we consider a Gaussian ridge $h_0 = 32\,\mathrm{m}$-tall and $4\sigma = 400\,\mathrm{m}$-wide in an ocean with a typical stratification $N = 10^{-3}\,\mathrm{rad/s}$. For a slow harmonic current with amplitude $u_0 = 1\,\mathrm{mm/s}$ flowing over this ridge at the semi-diurnal tidal frequency $\omega = 2\times10^{-4}\,\mathrm{rad/s}$, the relevant parameters are $\varepsilon = 0.95$, $ku_0/\omega = 0.0125$ and $\mathrm{Re} = 3.6\times10^5$. Figure 6-4b shows an analytical cross-beam profile of ΔN^2 close to the topography and at $\phi = \pi$. The negative perturbations of the buoyancy field are $\Delta N^2 = -1.07\times10^{-6}(\mathrm{rad/s})^2$ about the background stratification $N^2 = 10^{-6}(\mathrm{rad/s})^2$, and thus this beam would be slightly unstable. For a larger excursion parameter, which is the case for figure 6-4a, a stronger and therefore more unstable beam would be generated. Note typical tidal currents can be an order of magnitude higher than the value quoted here, typically $u_0 = 1\,\mathrm{cm/s}$, and also ocean ridges can be an order of magnitude wider. This in itself raises the Reynolds number to $O(10^7)$, where the effect of viscosity in the propagating beam would be negligible and a near critical topography would be likely to develop instabilities such as are predicted by the inviscid theory.

The onset of instability to vertical shear occurs for even less dramatic perturbations than yield buoyancy instabilities, when the Richardson number

$$Ri = \frac{N^2 + \Delta N^2}{(\partial u/\partial z)^2} < 1/4 \tag{6.2}$$

[19]. Therefore, shear instabilities are also predicted for topographies with high criticality. St. Laurent and Garrett [33] discuss instabilities to vertical shear in internal tides radiated from steep topography, and numerical studies by Khatiwala [16] show high shear locally over supercritical topographies. In the experiments, however, viscosity was significant enough to smooth out instability to shear along the wave beams. Figure 6-5 shows theoretical profiles of the density stratification $N^2 + \Delta N^2$, the square of the vertical shear $(\partial u/\partial z)^2$, and the Richardson number Ri along the cross section labelled 1 in figure 5-3 for the steep beam, knife-edge experiment. This corresponds to the experimental beam cross section with the highest disturbances, which was in good agreement with the theory. Clearly the stability of the density stratification is much stronger than the vertical shear. The Richardson number blows up when the shear is zero, and even at the locations where it is smallest, it is many orders of magnitude above 1/4.

The experimental perturbations were strongest closest to the knife-edge. If there were instabilities in the experimental wave field these would occur very close to the topography, where, for such large disturbances, neither the theory nor the experimental method is not necessarily accurate. Whether or not the flow was locally unstable, we did not see evidence of mixing even locally during the experiment.

In general, buoyancy or shear instabilities can lead to mixing either locally or in the radiated beam, which is an open question of much interest in oceanography. Linear theory suggests that the buoyancy disturbances are very sharp over steep topography (high criticality), such that instabilities will occur for strong (long excursion) tidal forcing. Indeed, as mentioned in the introduction, ocean observations of mixing have been reported locally over the Cobb seamount by Lueck and Mudge [23], over the Hawaiian ridge by Rudnick et. al. [32], and along wave beams radiated off the Monterey Bay by Lien and Gregg [20]; all near sites of supercritical generation. However, it has not been established which mechanism (whether buoyancy or shear) is in place in different cases. Neither of these instabilities or mixing is seen anywhere in the experimental

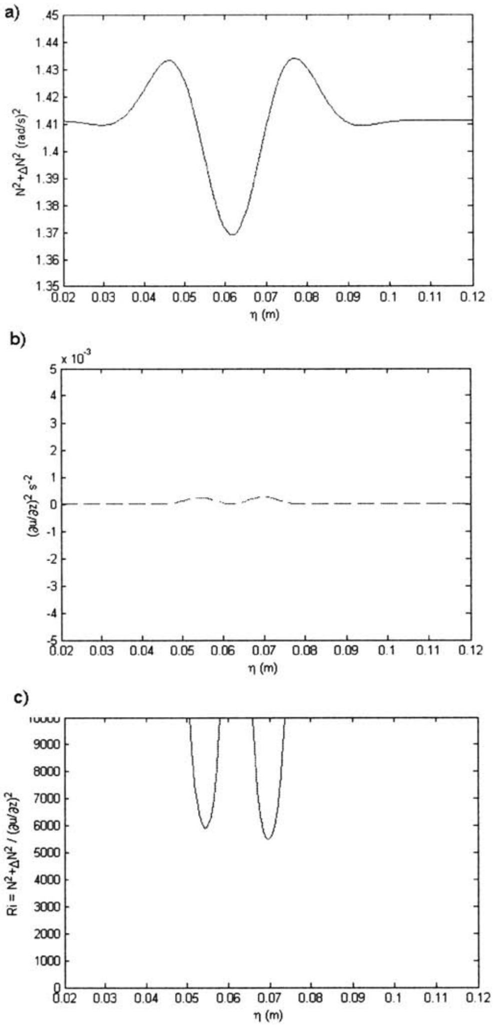

Figure 6-5: Profiles of a) stratification $N^2 + \Delta N^2$, b) square vertical shear $(\partial u/\partial z)^2$ and c) Richardson number Ri along cross section 1 in figure 5-6.

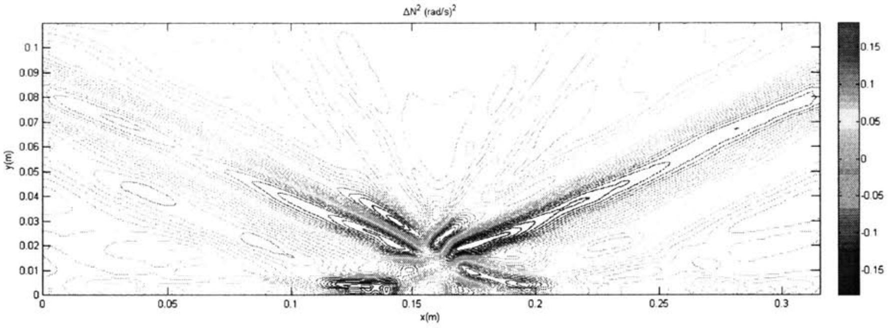

Figure 6-6: Full-frame contour plot of ΔN^2 in the wave field around a 25 ° beam. The forcing was $A = 2.55 \pm 0.05$ mm.

wave fields presented here, even for the supercritical problem, because viscosity smooths out the disturbances to the buoyancy field. These observations clearly indicate that it is important to consider the effect of Reynolds number when developing criteria for internal tide instabilities.

6.3 Visualizations of long excursion

The theoretical model for the knife-edge was based on a small excursion assumption that is not formally valid for this configuration. However, the experimental observations for excursion parameters $O(1)$ did not indicate nonlinear effects and still yield good agreement with theory. The discussion in section 6.2 suggests that this is due to the soothing action of viscosity. Since the knife-edge wave fields did show strong local disturbances, we investigated generation for stronger forcing, looking for the onset of nonlinear effects that might indicate the breakdown of theory. As the tidal excursion was increased, second harmonic beams became visible; and for even longer excursion the tidal flow started separating over the topography.

Figure 6-6 shows contours of ΔN^2 for the same experiment set up as figure 6-1, but with a forcing amplitude $A = 2.55 \pm 0.05\,\text{mm}$. The second harmonic beams in this wave field are clearly visible. Thus, second harmonic beams were only observed in the experiments if the excursion parameter was longer (high criticality alone was not enough), suggesting either that at small excursions the Reynolds number was so low that viscosity had a larger role damping local nonlinearities, or that the second harmonics were principally the result of a lee-wave mechanism

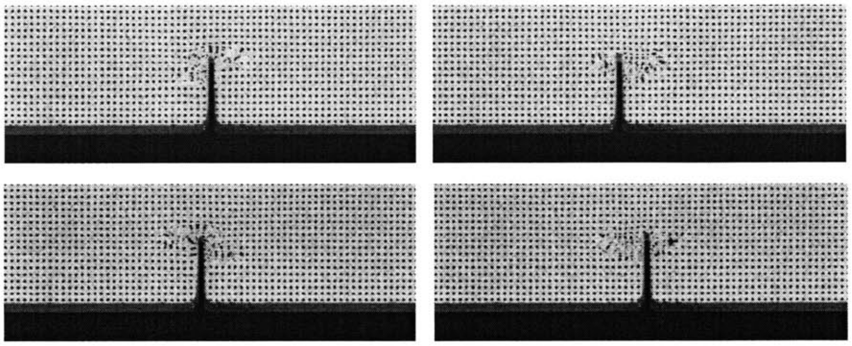

Figure 6-7: Snapshots of flow over the knife-edge. The forcing amplitude was $A = 2.55 \pm 0.05\,\mathrm{mm}$.

when the excursion was large, or a combination of both effects.

The strength of the disturbances over the topography for the experiment parameters in figure 6-6 can be appreciated more clearly in figure 6-7. This shows a sequence of snapshots of the distortions caused by the flow on a pattern of regular dots placed behind the tank, corresponding to $\phi = 0, \pi/2, \pi$ and $3\pi/2$ over one period of oscillation. The distortions are strong, and a streamline seems to separate and re-attach to the topography during the course of the oscillation. This is the first indication of flow separation in the experiment, which is expected for long excursion over a finite amplitude topographic feature, and which is certainly not accounted for in linear models of tidal conversion.

Bell's analytical solution for tidal conversion over weak topography allows for long excursion, which results in the generation of lee-waves; but there is no theory that predicts the tidal conversion by long excursion over finite amplitude topography. The experimental and field observations for these cases show boundary layer separation. Sutherland [36] performed a series of experiments with steady flow induced by towing periodic, steep topography across a stratification. Here boundary layer separation satisfied the criteria that the aspect ratio $h_0 k \gg 1$ and that the inverse Froude number $N h_0 / u_0 > 1$. This reduced the effective height of the topographies, so the internal wave field was weaker than expected. There have also been ocean observations of flow separation over steep topography by Farmer and Armi [6], as well as numerical simulations showing flow separation over the Knight inlet sill by Lamb [18] and

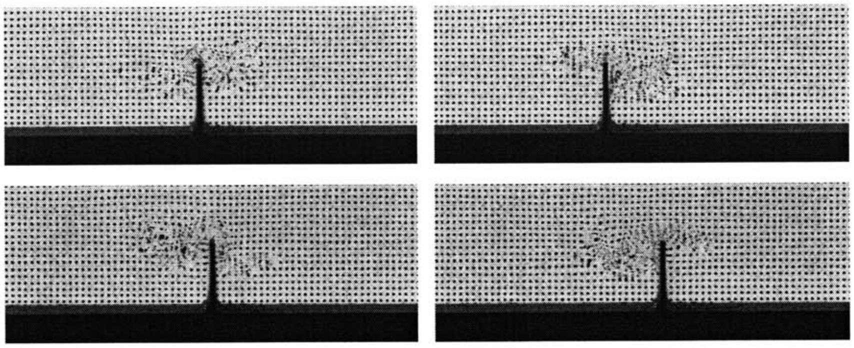

Figure 6-8: Snapshots of flow over the knife-edge. The forcing amplitude was $A = 7.00 \pm 0.05\,\mathrm{mm}$.

of flow separation caused by the Antarctic Circumpolar current by Ferrari [7]. Similar results should be expected for the experiments with harmonic forcing of sufficiently long excursion. Indeed, repeating the visualization in figure 6-7, this time for a forcing $A = 7.00 \pm 0.05\,\mathrm{mm}$, shows strong flow separation and possibly the onset of mixing, as seen in figure 6-8.

The long excursion parameter regime is ripe for experimental investigation. It is a regime in which nonlinearities arise and un-modelled mechanisms such as flow separation take place, both of which are of much interest in oceanography. Furthermore, neither theoretical or numerical approaches are well suited to study this regime due to its highly nonlinear behavior and the fine spatial structure of its features.

Many processes concerning nonlinear internal waves and long excursion parameters are not included in the scope of this work. An interesting example is the evolution in deep water of internal wave beams radiated from steep bathymetry into high frequency and large amplitude solitary internal waves. These have been observed in synthetic aperture radar satellite images (mostly ERS-SAR) around the world. Zhao et. al. [41] suggest that the solitary waves seen in the deep water basin of the South China Sea, are caused by nonlinear steepening of long excursion internal tides generated at the steep ridge across the Luzon Strait. Similarly, New and Da Silva [28] use remote sensing evidence of nonlinear waves in the central Bay of Biscayne to suggest that these evolve from internal wave beams generated at the steep shelf break.

Chapter 7

Conclusions

Internal tides are a key link in the energy transfer chain in the ocean: they draw energy from the barotropic tide and their eventual dissipation drives ocean circulation. In particular, the processes by which internal tides are generated determine the amount of energy transfer from the barotropic to the baroclinic tides, and generate instabilities that lead to overturning and mixing. Linear models have been used to estimate tidal conversion and they have been compared to numerical simulations and ocean observations of the energy flux (as reported by [1] and [16]); but there has been no experimental study of linear models.

A series of experiments were performed using the novel synthetic Schlieren measurement technique to simulate linear tidal conversion by two-dimensional topography. The two idealized topographies used were a knife-edge and a subcritical Gaussian ridge; and the results were compared with the predictions of existing theoretical models by Balmforth, Ierley and Young [1] and Hurley and Keady [15], respectively. Both models were corrected to account for the effect of viscosity in the propagating beams.

A linear density stratification was set up in a wave-tank and the topographic features were mounted on a sliding stage at the bottom of the tank and oscillated back and forth to simulate tidal currents over the topography. The wave fields generated were measured by capturing the distortion of a pattern of random dots behind the wave tank using a CCD camera, and using the synthetic Schlieren processing of the movies. Much care was taken to reduce noise in the experiment measurement and to accurately account for the different experimental parameters.

We compared experimental and theoretical cross-beam profiles of perturbations to the density gradient for wave beams generated at two different angles, for the two different topographies. In general, the agreement between experiment and theory is good and validates the linear theory that is used in ocean models. The results also show that viscosity plays an important role in tidal generation at lower Reynolds numbers. It enforces the linearity of the wave field over the knife-edge, and it has a moderate effect on the linear wave field over the Gaussian ridge. This suppresses nonlinear effects, allowing better agreement with linear models that are corrected for viscosity, and smoothens out instabilities predicted by inviscid models that would lead to overturning.

The experimental set up could be improved to investigate the nonlinear parameter regimes in which the linear models break down, aiming to improve ocean models. It would be desirable to perform experiments in a larger tank to achieve a higher Re and longer excursion parameters, in order to recreate instabilities and mixing that get smoothed out at lower Re. A problem of particular interest is the onset of flow separation at larger excursion parameters. Many numerical models of the ocean have bottom boundary conditions that allow slip, which does not allow flow separation; and this in turn affects tidal conversion, as shown by Sutherland's [36] experiments. Experiments can complement nonlinear numerical studies of internal tide generation, which generally do not allow high resolution of the wave field, and may be only weakly nonlinear [9]. Such considerations have motivated the construction of a larger tank that will also be fitted with a computer-controlled, double-bucket system capable of setting up nonlinear stratifications. Future experiments in the new system will investigate instabilities, flow separation and nonlinear stratifications, among other open issues regarding internal tide generation.

Bibliography

[1] N.J. Balmforth, G.R. Ierley and W.R. Young, Tidal conversion by nearly critical topography, J. Phys. Oceanogr. 32:2900-2914 (2002).

[2] T.H. Bell, Lee waves in stratified flows with simple harmonic time dependence, J. Fluid Mech. 67:705-722 (1975).

[3] D. A. Cacchione, L. F. Pratson, and A. S. Ogston, The shaping of continental slopes by internal tide. Science, 296:724–727 (2002).

[4] S. B. Dalziel, G. O. Hughes, B. R. Sutherland, Whole-field density measurements by 'synthetic Schlieren', Exp. Fluids 28:322-335 (2000).

[5] G.D. Egbert and R.D. Ray, Estimates of M_2 tidal dissipation from TOPEX/POSEIDON altimeter data. J. Geophys. Res. 106:22475-22502 (2001).

[6] D.M. Farmer and L. Armi, Stratified flow over topography: The role of small scale entrainment and mixing in flow establishment, Proc. Roy. Soc. Lond. 455A:3221-3258 (1999).

[7] R. Ferrari, Flow separation caused by the Antartic Circumpolar Current, personal communication.

[8] C. Garrett, Internal tides and ocean mixing, Science 301:1858–1859 (2003).

[9] C. Garrett and E. Kunze, Internal tide generation in the deep ocean, Ann. Rev. Fluid Mech., in preparation.

[10] D.F Hill, General density gradients in general domains: the "two-tank" method revisited, Expts. Fluids 32:434-440 (2002).

[11] P. E. Holloway, et. al., A Nonlinear Model of Internal Tide Transformation on the Australian North West Shelf, J. Phys. Oceanogr. 27:871-896 (1999)

[12] P.E. Holloway and M.A. Merrifield, Internal tide generation by seamounts, ridges and islands, J. Geo. Res. 104:25,937-25,951 (1999).

[13] Hawaii Ocean-Mixing Experiment (HOME) home-page, http://chowder.ucsd.edu/home/

[14] D.G Hurley and G. Keady. The generation of internal waves by vibrating elliptic cylinders. Part 1. Inviscid solution. J. Fluid Mech. 351:105-118 (1997).

[15] D.G Hurley and G. Keady. The generation of internal waves by vibrating elliptic cylinders. Part 2. Approximate viscous solution. J. Fluid Mech. 351:119–138 (1997).

[16] S. Khatiwala, Generation of internal tides in the ocean, Deep-Sea Res., 50:3-21 (2003).

[17] K.G. Lamb, Nonlinear interaction among internal wavebeams generated by tidal flow over supercritical topography, Geo. Res. Lett. 31:L09313 (2004).

[18] K.G. Lamb, On boundary-layer separation and internal wave generation at the Knight Inlet sill, Proc. R. Soc. Lon. 460:2305-2337 (2004).

[19] P. H. LeBlond, and L. A. Mysak, Waves in the Ocean. Elsevier (1978).

[20] R.C. Lien and M.C. Gregg, Observations of turbulence in a tidal beam and across a coastal ridge. J. Geophys. Res. 106:4575-4591 (2001).

[21] S.G. Llewllyn Smith and W.R. Young, Conversion of the barotropic tide, J. Phys. Oceanogr. 32:1554-1566 (2002).

[22] S.G. Llewellyn Smith and W.R. Young, Tidal conversion at a very steep ridge, J. Fluid Mech. 495:175-191 (2003).

[23] R.G. Lueck and T.D. Mudge, Topographically induced mixing around a shallow seamount, Science 276:1831-1833 (1997).

[24] J.A. MacKinnon and K.B. Winters, Subcritical catastrophe: Significant loss of low-mode tidal energy at 28.9 °, Geo. Res. Lett. 32:L15605 (2005).

[25] M.A. Merrifield and P.E. Holloway, Model estimates of M2 internal tide energetics at the Hawaiian Ridge, J. Geophys. Res. 107, C8, 10.1029 (2002).

[26] W. Munk and C. Wunsch, Abyssal recipes II: energetics of tidal and wind mixing, Deep-Sea Res., 45:1977-2010 (1998).

[27] J. D. Nash et. al. Internal Tide Reflection and Turbulent Mixing on the Continental Slope, J. Phys. Oceanogr. 34:1117-1134, (2004)

[28] A. L. New and J.C.B. Da Silva, Remote-sensing evidence for the local generation of internal soliton packets in the central Bay of Biscay. Deep-Sea Res. I 49:915–934 (2002).

[29] T. Peacock and P. Weidman, The effect of rotation on conical wavebeams in a stratified fuid, Expts. Fluids 39:32 (2005).

[30] F. Petrelis, S.G. Llewellyn Smith and W.R. Young, Tidal conversion at a submarine ridge, J. Fluid Mech., in press (2006).

[31] L. Rosenhead, Laminar Boundary Layers. Oxford University Press (1963).

[32] D.L. Rudnick et al. From tides to mixing along the Hawaiian Ridge, Science 301:355-357 (2003).

[33] L. St.Laurent and C. Garrett, The role of internal tides in mixing the deep ocean. J. Phys Oceanogr. 32:2882-2899 (2002).

[34] L. St.Laurent, S. Stringer, C. Garrett and D. Perrault-Joncas, The generation of internal tides at abrupt topography, Deep-Sea Res. 50:987-1003 (2003).

[35] B.R. Sutherland, S.B. Dalziel, G.O. Hughes and P.F. Linden, Visualization and measurement of internal waves by 'Synthetic Schlieren'. Part 1. Vertically oscillating cylinder, J. Fluid. Mech. 390:93-126 (1999).

[36] B. R. Sutherland and D. A. Aguilar, Stratified Flow over Topography: Wave Generation and Boundary Layer Separation, submitted to Advances in Fluid Mechanics, WIT Press (2006).

[37] N.H. Thomas and T. N. Stevenson, A similarity solution of viscous internal waves. J. Fluid Mech. 54:495-506 (1972)

[38] G. Veronis, On the approximations in transforming the equations of motion from a spherical surface to the β-plane. II. Baroclinic systems. J. Mar. Res., 24:338-349 (1936)

[39] R. C. Weast, Handbook of chemistry and physics, C.R.C. Press, 62 edition (1981).

[40] C. Wunsch and R. Ferrari, Vertical mixing, energy, and the general circulation of the oceans. Ann. Rev. Fluid Mech. 36:281–314 (2004).

[41] Z. Zhao, V. Klemas, Q. Zheng and X.-H. Yan, Remote sensing evidence for baroclinic tide origin of internal solitary waves in the northeastern South China Sea, Geo. Res. Lett. 31:L06302 (2004).